ACS Catalysis

pubs.acs.org/acscatalysis

Perspective

Materials Screening by the Descriptor $G_{max}(\eta)$: The Free-Energy Span Model in Electrocatalysis

Samad Razzaq and Kai S. Exner*

Cite This: *ACS Catal.* 2023, 13, 1740−1758

Read Online

ACCESS | Metrics & More | Article Recommendations

ABSTRACT: To move from fossil-based energy resources to a society based on renewables, electrode materials free of precious noble metals are required to efficiently catalyze electrochemical processes in fuel cells, batteries, or electrolyzers. Materials screening operating at minimal computational cost is a powerful method to assess the performance of potential electrode compositions based on heuristic concepts. While the thermodynamic overpotential in combination with the volcano concept refers to the most popular descriptor-based analysis in the literature, this notion cannot reproduce experimental trends reasonably well. About two years ago, the concept of $G_{max}(\eta)$, based on the idea of the free-energy span model, has been proposed as a universal approach for the screening of electrocatalysts. In contrast to other available descriptor-based methods, $G_{max}(\eta)$ factors overpotential and kinetic effects by a dedicated evacuation scheme of adsorption free energies into an analysis of trends. In the present perspective, we discuss the application of $G_{max}(\eta)$ to different electrocatalytic processes, including the oxygen evolution and reduction reactions, the nitrogen reduction reaction, and the selectivity problem of the competing oxygen evolution and peroxide formation reactions, and we outline the advantages of this screening approach over previous investigations.

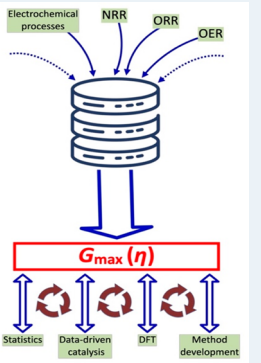

KEYWORDS: *oxygen electrocatalysis, nitrogen reduction reaction, scaling relation, bifunctional index, descriptor-based approach, microkinetic modeling, multidimensional database, data-driven electrocatalysis*

1. INTRODUCTION

Coal, oil, and natural gas are still the major contributors to global energy production. These conventional, nonrenewable resources are hazardous and environmentally unfriendly because they release toxic elements upon their production and consumption. Besides the environmental consequences, they are being depleted while human demand for energy is ever-increasing.[1−3] Hence, energy production from renewables is needed, but most of these sources such as wind, tidal, and solar powers are intermittent. Therefore, energy storage is ultimately called for, implying that overproduced energy can be stored in chemical bonds, such as gaseous hydrogen (H_2), and that in the case of an energy deficit the storage system can feed the grid with the required electricity.[4−6] Vital electrochemical devices for energy conversion and storage are fuel cells, electrolyzers, and batteries, which, in the long run, are thought to maintain the necessities of our everyday life, such as mobility, communication, transmission, and industrial manufacturing. At the electrodes in these devices, electrochemical reactions take place. For example, oxygen electrocatalysis comprising the oxygen evolution (OER) and oxygen reduction reactions (ORR) is operative at the cathode of metal−air batteries,[7−9] while in electrolyzers the hydrogen evolution (HER) and oxygen evolution reactions (OER) take place at the cathode and anode, respectively.[10−12] Likewise, fuel cells convert chemical energy into electrical energy by the anodic hydrogen oxidation reaction (HOR) and cathodic ORR.[13−15] To design an electrode material with improved performance, an atomic-scale understanding of these electrochemical reactions is ultimately needed.

With the advancement of computational capacities in the 21st century, a remarkable amount of work has been dedicated to *in silico* catalyst design for these reactions using electronic structure calculations in the density functional theory (DFT) approximation. The ultimate goal of these studies is to connect the microscopic picture (elementary reaction steps modeled by DFT) with the macroscopic picture in terms of experimental observations. Commonly, free-energy diagrams (FEDs) are used to build a bridge between these two worlds.[16,17] In theory, the elementary steps of an electrochemical process with N electron transfers consist of at least of $N - 1$ reaction intermediates (RIs) and N transition states (TSs) (cf. Figure 1a). Modeling the entire FED is mathematically exact; yet, it is computationally expensive and not feasible for the investigation of a plethora of different electrode compositions,

Received: August 12, 2022
Revised: December 5, 2022
Published: January 17, 2023

https://doi.org/10.1021/acscatal.2c03997
ACS Catal. 2023, 13, 1740−1758

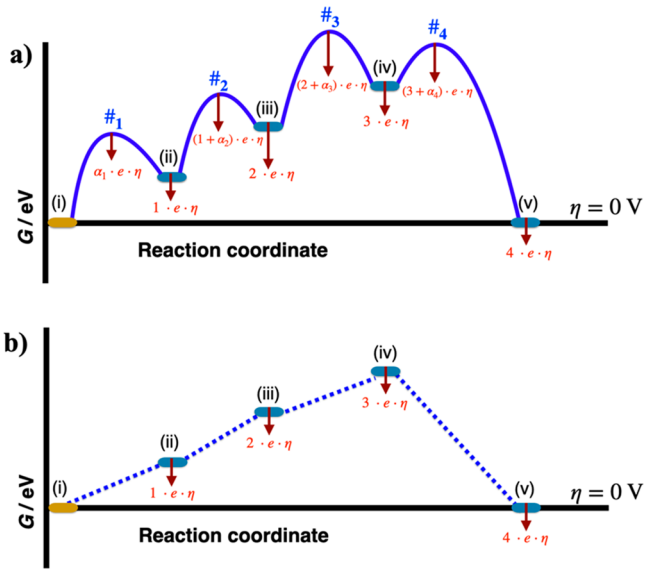

Figure 1. (a) Free-energy diagram (FED) of a four-electron process comprising four transition states (TSs), $\#_j$ (j = 1, 2, 3, 4), and the associated reaction intermediates (RIs), denoted (i)−(v), under equilibrium conditions (η = 0 V). The RI with the lowest free energy is indicated in yellow. Brown arrows specify the overpotential dependence of each RI and TS, while α_j (j = 1, 2, 3, 4) denotes the transfer coefficient of each TS. (b) Simplification of the same electrochemical reaction by neglecting the TS. Commonly, only the energetics of the RIs are analyzed to assess the electrocatalytic activity in a heuristic fashion by high-throughput approaches.

which, however, is needed to identify suitable candidates within the large phase space of available materials. Therefore, the high-throughput screening of catalysts in a homologous series of materials is based on a heuristic approach in that only the RIs (thermodynamics) in the FED are calculated whereas the TSs (kinetics) are neglected, as shown in Figure 1b.

The first attempt of a heuristic theory for the screening of electrocatalysts applied to energy storage and conversion processes was formulated by Nørskov and co-workers, who introduced the concept of the computational hydrogen electrode (CHE)[18] and the thermodynamic overpotential, η_{TD},[18,19] as an activity descriptor. The methodology put forth by Nørskov and co-workers extends the Anderson−Newns model[20] by computing the adsorption free energies of the RIs using DFT. While in their initial benchmark work the ORR was studied,[18] in the following, we refer to the OER[21,22] in this perspective. The mononuclear OER mechanism, which consists of the same adsorbates as the suggested ORR mechanism, is given by eqs 1−4:

$$\mathrm{M} + \mathrm{H_2O_{(l)}} \rightarrow \mathrm{M{-}OH} + \mathrm{H^+} + \mathrm{e^-} \qquad \Delta G_1^{\mathrm{OER}} \qquad (1)$$

$$\mathrm{M{-}OH} \rightarrow \mathrm{M{-}O} + \mathrm{H^+} + \mathrm{e^-} \qquad \Delta G_2^{\mathrm{OER}} \qquad (2)$$

$$\mathrm{M{-}O} + \mathrm{H_2O_{(l)}} \rightarrow \mathrm{M{-}OOH} + \mathrm{H^+} + \mathrm{e^-} \qquad \Delta G_3^{\mathrm{OER}} \qquad (3)$$

$$\mathrm{M{-}OOH} \rightarrow \mathrm{M} + \mathrm{O_{2(g)}} + \mathrm{H^+} + \mathrm{e^-} \qquad \Delta G_4^{\mathrm{OER}} \qquad (4)$$

M denotes the catalytically active surface site, and the $\Delta G_{j=1,2,3,4}^{\mathrm{OER}}$ values refer to the free-energy changes of the respective proton−electron (H^+/e^-) transfer steps in the OER mechanism. The free energies of H^+ and e^- are referred to half of the free energy of a hydrogen molecule by the CHE approach (cf. eqs 5 and 6), which enables using a reference accessible to gas-phase DFT to study the energetics of adsorbate species at electrified interfaces.

$$\mathrm{H^+} + \mathrm{e^-} \rightleftharpoons \frac{1}{2}\mathrm{H_{2(g)}}\ @U = 0\ \mathrm{V\ vs\ RHE} \qquad (5)$$

$$\tilde{\mu}_{\mathrm{H^+}} + \tilde{\mu}_{\mathrm{e^-}} = \frac{1}{2}G(\mathrm{H_2}) \qquad (6)$$

Note that the use of the CHE approach implies that electrons and protons are transferred in concert rather than in a decoupled fashion, and DFT calculations are carried out in a canonical ensemble (fixed charge) rather than in a grand canonical ensemble with constant electrode potential; the latter refers to the experimental conditions.[23,24] The CHE model can be used to obtain the free-energy change for each electrochemical step according to eq 7:[25]

$$\Delta G_x/\mathrm{eV} = \Delta E_{\mathrm{DFT}} + \Delta \mathrm{ZPE} - T\Delta S - eU - 0.059 \times \mathrm{pH} \qquad (7)$$

Equation 7 allows deriving the $\Delta G_{j=1,2,3,4}^{\mathrm{OER}}$ values of the OER mechanism at any applied electrode potential, U, and pH in that only the adsorption energies (ΔE_{DFT}), zero-point energies (ΔZPE), and entropy changes (ΔS) are evaluated based on DFT calculations or thermodynamic data tables at T = 298.15 K, respectively. It should be noted that, due to the fundamental laws of equilibrium thermodynamics, the free-energy changes associated with the 3 RIs (OH, O, and OOH) sum up to 4.92 eV:

$$\begin{aligned} &\Delta G_1^{\mathrm{OER}} + \Delta G_2^{\mathrm{OER}} + \Delta G_3^{\mathrm{OER}} + \Delta G_4^{\mathrm{OER}} \\ &= 4.92\ \mathrm{eV} \\ &= 4 \times e \times U_{\mathrm{OER}}^0 \end{aligned} \qquad (8)$$

Knowledge of the $\Delta G_{j=1,2,3,4}^{\mathrm{OER}}$ values allows classifying materials into active and inactive catalysts by using the Sabatier principle and the Brønsted−Evans−Polanyi relation. In this context, the Sabatier principle states that the RIs should be bound neither too strongly nor too weakly to the catalyst surface.[26] Yet, the Sabatier principle does not make any quantitative statement on the RIs' binding energies.[27]

The thermodynamic overpotential, η_{TD}, as an activity descriptor relies on a combination of the Sabatier principle and the Brønsted−Evans−Polanyi (BEP) relation[28] by evaluating the highest free-energy change among the set of all free-energy changes at zero overpotential, $\eta = U - 1.23$ V:

$$\eta_{\mathrm{TD}} = \max\left\{\frac{\Delta G_j - 1.23\ \mathrm{V}}{e}\right\} \quad j = 1, 2, 3, 4 \qquad (9)$$

The reasoning of this descriptor is as follows: the smaller the value of η_{TD}, the higher the activity of a catalyst. η_{TD} is a very simple descriptor that enables materials screening by the assessment of a single free-energy change. Based on this notion, new electrode compositions could be identified for electrocatalytic processes, such as MoS_2 for the HER[29−35] or $IrO_x/SrIrO_3$ for the OER.[36] However, both theoreticians and experimentalists have severely criticized the usage of η_{TD} recently because trends in a homologous series of materials cannot always be captured correctly by this descriptor.[37−40] The elementary step that defines η_{TD} is denoted as the potential-determining step (PDS). Electrocatalytic activity, however, is governed by the rate-determining step (RDS), which remains unknown in the thermodynamic picture of

https://doi.org/10.1021/acscatal.2c03997
ACS Catal. 2023, 13, 1740−1758

adsorption energies because TSs are not explicitly investigated. As a fundamental consequence, the concept of η_{TD} relies on the tacit assumption that the condition PDS = RDS is met;[41−43] however, the PDS does not necessarily correspond to the RDS, as exemplarily shown in Figure 2.

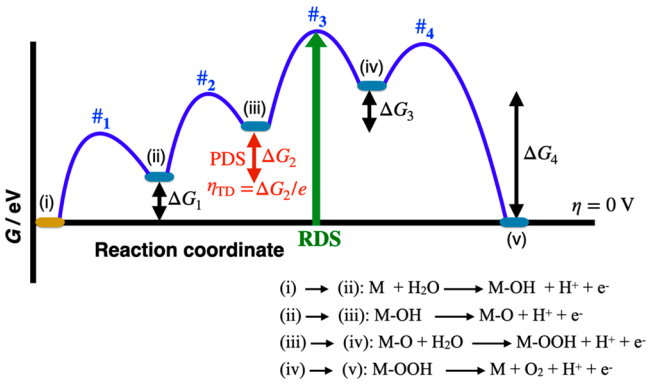

Figure 2. FED of the OER according to the mechanistic description in eqs 1−4 under equilibrium conditions (η = 0 V). The thermodynamic overpotential, η_{TD}, evaluates the largest free-energy change ($\Delta G^{OER}_{j=1,2,3,4}$) of the elementary reaction steps at zero overpotential to approximate electrocatalytic activity by the concept of the PDS but neglects the kinetics in terms of the TSs $\#_{j=1,2,3,4}$. In contrast, the RDS is given by the transition (i) → $\#_3$, indicating that the PDS and RDS do not match.

Therefore, the simplicity of η_{TD} by focusing on the thermodynamic picture while the kinetics is ignored is identified as the main reason activity trends are not always reproduced correctly by this descriptor. More precisely, η_{TD} is a powerful approach to identify inactive catalysts at the leg of a volcano plot,[44−47] but it is a weak descriptor to distinguish between active and highly active materials or to sort catalysts according to their activity.[48,49] Given that our main interest is dedicated to active materials rather than inactive catalysts, this finding calls for the development of advanced concepts that build upon the two major weaknesses of the descriptor η_{TD}:

(i) The entire analysis is carried out at the equilibrium potential of the reaction, η_{OER} = 0 V, whereas experiments quantify production formation only for η_{OER} > 0 V.
(ii) The entire analysis relies on adsorption free energies whereas the kinetics is ignored.

The first aspect can be solved by shifting the reference potential in the analysis in that trends are analyzed under OER conditions (e.g., η_{OER} = 0.3 V) rather than at η_{OER} = 0 V.[50,51] The second aspect is more difficult, given that an explicit calculation of the kinetics is still computationally too expensive for catalyst screening.[52−55] However, the concept of the free-energy span model,[56,57] as introduced by Kozuch and Shaik in homogeneous catalysis, is a potential opportunity to build a bridge between the thermodynamics in terms of binding energies and the kinetics governing the electrocatalytic activity. Both aspects were taken up by Exner to introduce an advanced descriptor for the high-throughput screening, denoted as $G_{max}(\eta)$.[43,58] We emphasize that also other descriptors besides the notion of $G_{max}(\eta)$ to capture activity trends for electrocatalytic processes have been postulated, such as the electrochemical-step symmetry index (ESSI),[59] the electrochemical-step asymmetry index (ESAI),[60,61] and G_{max}.[62] The present perspective focuses solely on the approach of $G_{max}(\eta)$ and its implications for energy conversion and storage processes. In the further course of this article, we will first introduce the activity descriptor $G_{max}(\eta)$ (section 2) and, after that, discuss its application to selected examples including the OER (section 3.1), bifunctional oxygen electrocatalysis (section 3.2), the selectivity challenge of the competing OER and peroxide formation (section 3.3), and the nitrogen reduction reaction (section 3.4).

2. $G_{max}(\eta)$: A UNIVERSAL ACTIVITY DESCRIPTOR FOR THE EVALUATION OF TRENDS

2.1. Mathematical Formalism. The descriptor $G_{max}(\eta)$ advances the free-energy span model, suggested by Kozuch and Shaik for homogeneous catalysis,[56] toward its applications in electrocatalysis, thereby accounting for the applied overpotential and kinetics effects in the analysis.[43,58] Considering the same OER mechanism as discussed in the Introduction (cf. eqs 1−4), the idea of this descriptor, also denoted as $G_{max}(U)$, relies on a potential-dependent description of the RIs' free energies (cf. eqs 10−14).

$$G_{M}(U) = 0 \tag{10}$$

$$G_{M-OH}(U) = \Delta G_1 - 1 \times e \times U \tag{11}$$

$$G_{M-O}(U) = \Delta G_1 + \Delta G_2 - 2 \times e \times U \tag{12}$$

$$G_{M-OOH}(U) = \Delta G_1 + \Delta G_2 + \Delta G_3 - 3 \times e \times U \tag{13}$$

$$G_{M+O_2}(U) = 4.92\ \text{eV} - 4 \times e \times U \tag{14}$$

$G_{max}(U)$ is then defined as the largest free-energy span between the RIs (cf. eqs 15−25) at a predefined target overpotential, $\eta = U - 1.23$ V, with $U > 1.23$ V vs RHE. In total, ten free-energy spans between the RIs are conceivable:

$$G_{span\#1}(U) = G_{M+O_2}(U) - G_{M-OOH}(U) \tag{15}$$

$$G_{span\#2}(U) = G_{M+O_2}(U) - G_{M-O}(U) \tag{16}$$

$$G_{span\#3}(U) = G_{M+O_2}(U) - G_{M-OH}(U) \tag{17}$$

$$G_{span\#4}(U) = G_{M+O_2}(U) - G_{M}(U) \tag{18}$$

$$G_{span\#5}(U) = G_{M-OOH}(U) - G_{M-O}(U) \tag{19}$$

$$G_{span\#6}(U) = G_{M-OOH}(U) - G_{M-OH}(U) \tag{20}$$

$$G_{span\#7}(U) = G_{M-OOH}(U) - G_{M}(U) \tag{21}$$

$$G_{span\#8}(U) = G_{M-O}(U) - G_{M-OH}(U) \tag{22}$$

$$G_{span\#9}(U) = G_{M-O}(U) - G_{M}(U) \tag{23}$$

$$G_{span\#10}(U) = G_{M-OH}(U) - G_{M}(U) \tag{24}$$

Equations 15−24 and the definition of $G_{max}(\eta)$ can be written in a compact format as

$$G_{max}(\eta) = \max\{G_{span\#k}(U),\ k = 1,\ \ldots,\ n\} \tag{25}$$

In eq 25, n represents the total number of plausible free-energy spans, which is strongly dependent on the number of intermediate states. In the case of 3 reaction intermediates, as encountered for the OER, 10 free-energy spans are observed.

https://doi.org/10.1021/acscatal.2c03997
ACS Catal. 2023, 13, 1740−1758

For even more complicated electrocatalytic processes, such as the nitrogen reduction reaction with five intermediate states, the number of possible free-energy spans amounts to 20.[63] We refer to the Supporting Information files of refs 43 and 63 for a detailed discussion of how to determine the respective free-energy spans for electrocatalytic reactions comprising a varying number of proton−electron coupled transfer steps.

A schematic illustration of how to evaluate $G_{max}(\eta)$ in a FED is illustrated in Figure 3. $G_{max}(\eta)$ approaches the rate-determining transition state ($G^{\#}_{RDS}$) and thus mimics overpotential and kinetic effects in the analysis of trends. The term $\Delta G^{\#}_{RDS\text{-}max}$, which is related to the free-energy difference between the TS with the highest free energy and the descriptor $G_{max}(\eta)$, is not accounted for in the analysis; however, it has been shown that the term $\Delta G^{\#}_{RDS\text{-}max}$ is a constant among different materials with a sensitivity of about 0.2 eV, and thus, $G_{max}(\eta)$ allows evaluating trends with an uncertainty of 0.2 eV.[43,58] A detailed description of how to apply the notion of $G_{max}(\eta)$ for the assessment of electrocatalytic activity is given in the Supporting Information of ref 43.

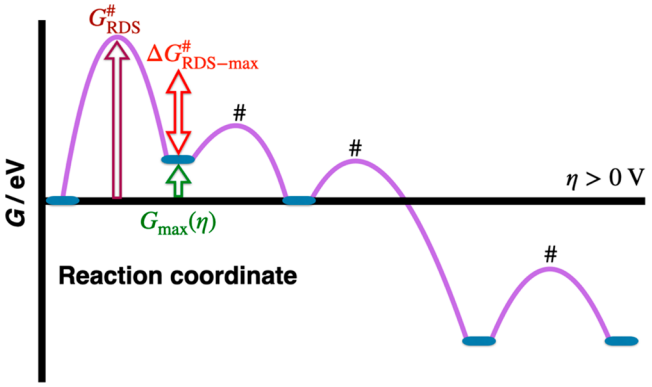

Figure 3. Schematic representation of a FED at a finite overpotential, $\eta > 0$ V, for an electrocatalytic process, such as the OER. RIs and transition states are indicated by solid blue lines and #, respectively. The descriptor $G_{max}(\eta)$ approaches the rate-determining transition state, $\#_{RDS}$, by computing the maxima of all plausible free-energy spans between the RIs (cf. eq 25). The meaning of the term $\Delta G^{\#}_{RDS\text{-}max}$ is further explained in section 2.3. Reproduced with permission from ref 64.

So far, we have described the mathematical formalism to compute $G_{max}(\eta)$ for an electrochemical reaction from the example of the OER. It is evident that the computational cost for the determination of $G_{max}(\eta)$ is the same as that of η_{TD}. Differences between $G_{max}(\eta)$ and η_{TD}, however, refer to the meaningfulness of these descriptors. While η_{TD} yields information on the PDS alone, the free-energy span model of $G_{max}(\eta)$ indispensably approaches the RDS for typical reaction conditions (cf. Figure 3) and thus is much closer to the actual rate-determining states than is η_{TD}. Furthermore, the notion of $G_{max}(\eta)$ can distinguish between electrochemical and chemical steps in a reaction mechanism, whereas chemical steps need to be connected to the subsequent electrochemical step on applying the descriptor η_{TD}. To extend this discussion, we compare $G_{max}(\eta)$ and η_{TD} in the OER for a reaction mechanism that contains both chemical and electrochemical steps.

2.2. $G_{max}(\eta)$ vs η_{TD} for Chemical and Electrochemical Reaction Steps. The conventional mononuclear mechanism for the OER contains the OH, O, and OOH adsorbates. Alternatively, bifunctional and binuclear OER mechanisms have been proposed in the literature.[44,65] Among these three anticipated mechanisms, the last two both consist of electrochemical and chemical reaction steps. The binuclear mechanism reads:

$$M + M + H_2O_{(l)} \rightarrow M{-}OH + M + H^+ + e^- \quad \Delta G_1^{OER} \quad (26)$$

$$M{-}OH + M \rightarrow M{-}O + M + H^+ + e^- \quad \Delta G_2^{OER} \quad (27)$$

$$M{-}O + M + H_2O_{(l)} \rightarrow M{-}O + M{-}OH + H^+ + e^- \quad \Delta G_3^{OER} \quad (28)$$

$$M{-}O + M{-}OH \rightarrow M{-}O + M{-}O + H^+ + e^- \quad \Delta G_4^{OER} \quad (29)$$

$$M{-}O + M{-}O \rightarrow M + M + O_2 \quad \Delta G_{chem}^{OER} \quad (30)$$

Equation 30 indicates the recombination of two neighboring oxygen surface atoms to form gaseous oxygen, which is a chemical reaction step without charge transfer. At $U = 0$ V vs RHE, the five free-energy changes of eqs 26−30 sum up to 4.92 eV to meet the requirements of equilibrium thermodynamics:

$$\Delta G_1^{OER} + \Delta G_2^{OER} + \Delta G_3^{OER} + \Delta G_4^{OER} + \Delta G_{chem}^{OER} = 4.92 \text{ eV} \quad (31)$$

For the application of η_{TD}, one needs to combine the chemical and electrochemical steps of eqs 29 and 30 so that the precondition of an electrochemical step is met:

$$M{-}O + M{-}OH \rightarrow M + M + O_{2(g)} + H^+ + e^- \quad \Delta G_{4,rev}^{OER} \quad (32)$$

Hence, η_{TD} assesses electrocatalytic activity by evaluating the free-energy changes ΔG_1^{OER}, ΔG_2^{OER}, ΔG_3^{OER}, and $\Delta G_{4,rev}^{OER}$ using eq 9. An example of an arbitrary FED of the binuclear OER mechanism is given in Figure 4. There, it becomes obvious that η_{TD} is defined by the free-energy change ΔG_1^{OER}. Yet, the thermodynamic FED of Figure 4 also indicates that ΔG_4^{OER} (cf. eq 29) corresponds to the elementary step that is the most uphill in free energy, but this finding cannot be captured by the notion of η_{TD} because ΔG_4^{OER} and ΔG_{chem}^{OER} are conjoined to $\Delta G_{4,rev}^{OER}$ (cf. eq 32). Therefore, it is viable to use an activity descriptor that can factor nonelectrochemical steps into the

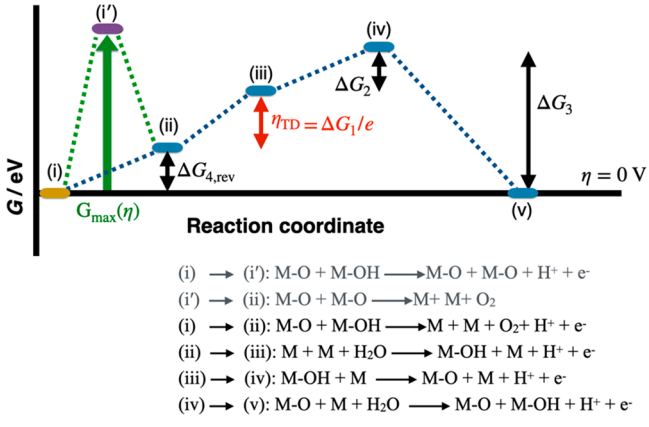

Figure 4. FED for the OER according to the binuclear pathway in eqs 26−30 at zero overpotential. The reaction steps (i) → (i′) and (i′) → (ii) are hidden on evaluating electrocatalytic activity by the concept of η_{TD} (purple). In contrast to this, the descriptor $G_{max}(\eta)$ is able to include chemical reaction steps in the evaluation of activity trends, identifying that the transition (i) → (i′) corresponds to the largest free-energy span along the reaction mechanism (green arrow).

https://doi.org/10.1021/acscatal.2c03997
ACS Catal. 2023, 13, 1740−1758

analysis of activity trends. Recalling that $G_{max}(\eta)$ relies on analyzing all possible free-energy spans within the reaction mechanism, this concept can also be exerted to chemical steps. For the binuclear OER mechanism, the corresponding free-energy spans are given by eqs 33−47:

$$G_{span\#1}(U) = G_{M+M+O_2}(U) - G_{M-O+M-O}(U) \quad (33)$$

$$G_{span\#2}(U) = G_{M+M+O_2}(U) - G_{M-O+M-OH}(U) \quad (34)$$

$$G_{span\#3}(U) = G_{M+M+O_2}(U) - G_{M-O+M}(U) \quad (35)$$

$$G_{span\#4}(U) = G_{M+M+O_2}(U) - G_{M-OH+M}(U) \quad (36)$$

$$G_{span\#5}(U) = G_{M+M+O_2}(U) - G_{M+M}(U) \quad (37)$$

$$G_{span\#6}(U) = G_{M-O+M-O}(U) - G_{M-O+M-OH}(U) \quad (38)$$

$$G_{span\#7}(U) = G_{M-O+M-O}(U) - G_{M-O+M}(U) \quad (39)$$

$$G_{span\#8}(U) = G_{M-O+M-O}(U) - G_{M-OH+M}(U) \quad (40)$$

$$G_{span\#9}(U) = G_{M-O+M-O}(U) - G_{M+M}(U) \quad (41)$$

$$G_{span\#10}(U) = G_{M-O+M-OH}(U) - G_{M-O+M}(U) \quad (42)$$

$$G_{span\#11}(U) = G_{M-O+M-OH}(U) - G_{M-OH+M}(U) \quad (43)$$

$$G_{span\#12}(U) = G_{M-O+M-OH}(U) - G_{M+M}(U) \quad (44)$$

$$G_{span\#13}(U) = G_{M-O+M}(U) - G_{M-OH+M}(U) \quad (45)$$

$$G_{span\#14}(U) = G_{M-O+M}(U) - G_{M+M}(U) \quad (46)$$

$$G_{span\#15}(U) = G_{M-OH+M}(U) - G_{M+M}(U) \quad (47)$$

The free-energy span model purports that $G_{span\ \#6}(U)$ (cf. eq 38) is reconciled with the descriptor $G_{max}(\eta)$. In contrast, when using the concept of η_{TD}, one would refer to $G_{span\ \#15}(U)$ (cf. eq 47). As shown in previous works, optimizing a free-energy change that does not correspond to the RDS may cause electrocatalysts to be optimized in the wrong direction toward lower activity.[66,67] This finding can be seen as the main reason the concept of $G_{max}(\eta)$ excels over the notion of η_{TD} for a thorough assessment of activity trends because various pathways, comprising both electrochemical and chemical steps, can be thoroughly evaluated in the mechanistic description to approach the RDS, thereby using simple thermodynamic considerations analyzed by a dedicated evaluation scheme.

2.3. Microkinetic Modeling by the Concept of $G_{max}(\eta)$.

In the Introduction, we have outlined two major shortcomings of the concept of η_{TD}, relating to overpotential and kinetic aspects in the evaluation of trends. While in the previous two subsections we have described how the descriptor $G_{max}(\eta)$ accounts for the potential dependence in the analysis, in the following, we refer to the kinetics. Even if $G_{max}(\eta)$ evaluates the largest free-energy span from the RI with smallest free energy to the RI with highest free energy, the electrocatalytic activity is governed by the TS with the highest free energy, $G^{\#}_{RDS}$ (cf. Figure 3). Figure 3 illustrates that $G_{max}(\eta)$ does not capture the free-energy difference between the RI with the highest free energy and the the transition state with the highest free energy in the analysis, denoted as $\Delta G^{\#}_{RDS\text{-}max}$. Henceforth, we are going to outline how $G_{max}(\eta)$ can be connected to $G^{\#}_{RDS}$ so that this activity descriptor can be used for microkinetic modeling.

Starting from the generalized Butler−Volmer equation in the Tafel approximation, the current density as a function of the applied overpotential is given by eq 48:[16,17]

$$j(\eta) = f(G^{\#}_{rds}, \beta_{RDS}) \approx \frac{4k_BT}{h} e\Gamma_{act} e^{-G^{\#}_{RDS}/k_BT} e^{+\beta_{RDS} e\eta/k_BT} \quad (48)$$

In eq 48, e, k_B, T, and h denote the elementary charge, the Boltzmann constant, the absolute temperature in Kelvin, and the Planck constant, respectively, while Γ_{act} represents the number of active sites per unit surface area. β_{RDS} corresponds to the apparent transfer coefficient and indicates the number of electrons transferred from the starting surface (RI with lowest free energy) to the transition state with the highest free energy.[16,68] For a fixed overpotential, η_{target}, eq 48 can be translated to eq 49 by making use of the relation in eq 50:

$$j(\eta_{target}) = f(G^{\#}_{RDS}(\eta_{target})) = \frac{4k_BT}{h} e\Gamma_{act} e^{-G^{\#}_{RDS}(\eta_{target})/k_BT} \quad (49)$$

$$G^{\#}_{RDS}(\eta_{target}) = G^{\#}_{RDS} - \beta_{RDS} e\eta_{target} \quad (50)$$

In previous works by Exner, it was demonstrated that there is an internal BEP relation between $G^{\#}_{RDS}(\eta)$ and $G_{max}(\eta)$:[43,58]

$$G^{\#}_{RDS}(\eta) = G_{max}(\eta) + \Delta G^{\#}_{RDS\text{-}max} \quad (51)$$

The term $\Delta G^{\#}_{RDS\text{-}max}$ (cf. Figure 3) is a potential-independent constant with a sensitivity of about 0.2 eV,[43] and thus, $G_{max}(\eta)$ directly scales with $\Delta G^{\#}_{RDS}(\eta)$, irrespective of the applied driving force:

$$G^{\#}_{RDS}(\eta) \approx G_{max}(\eta) + \text{constant} \quad (52)$$

Inserting eq 52 into eq 49, it becomes evident that the current density, $j(\eta_{target})$, can be approximated by the descriptor $G_{max}(\eta)$ if one is using an educated guess for the constant of eq 52:

$$j(\eta_{target}) = \frac{4k_BT}{h} e\Gamma_{act} e^{-(G_{max}(\eta_{target}) + \text{constant})/k_BT} \quad (53)$$

Previous studies have shown that one may apply a value range between 0.4 and 0.6 eV as lower and upper bounds for the constant, respectively.[43]

It is noteworthy that the approximation of current densities for electrocatalytic processes as a function of the applied overpotential goes far beyond the notion of η_{TD}. In the case of η_{TD}, it has been reported that theoretically calculated values scale with the experimental overpotential to reach 10 mA/cm^2 in a homologous series of materials.[69] Yet, it would be incorrect to relate η_{TD} to any experimental current density because there is no direct connection between the descriptor η_{TD} and the electrocatalytic rate. Instead, η_{TD} is an educated guess to comprehend trends by relying on the tacit assumption of PDS = RDS.[41−43,62] The notion of $G_{max}(\eta)$ allows an approximation of current densities, but only if the constant in the numerator of the exponential term (cf. eq 53) is accounted for. Therefore, determining current densities by $G_{max}(\eta)$ is possible in a qualitative rather than in a quantitative fashion. Yet, this approach can be used to study the upper and lower boundaries of current densities for electrochemical processes dependent on the driving force, which can help to rationalize

https://doi.org/10.1021/acscatal.2c03997
ACS Catal. 2023, 13, 1740−1758

trends. We use this methodology to discuss the bifunctional oxygen electrocatalysis and the selectivity problem of the oxygen evolution and peroxide formation reactions in sections 3.2 and 3.3, respectively.

2.4. Approaching the Rate-Determining Step by the Concept of $G_{max}(\eta)$. The concept of the thermodynamic overpotential, η_{TD}, has spurred materials screening by resolving the potential-determining step (PDS) of a mechanistic description.[41−43,62] The PDS refers to the elementary reaction step with the highest free-energy change at zero overpotential (cf. Figure 2). However, as pointed out by Koper for the simple HER, the PDS may differ from the actual RDS governing the rate of the reaction.[41] Exner gave further evidence on the potential-dependent relationship of the PDS and RDS, outlining that for small overpotentials the PDS may differ from the RDS, whereas for large overpotentials the PDS may approach the RDS.[43]

A peculiarity of the descriptor $G_{max}(\eta)$ refers to the fact that this activity measure can resolve the actual RDS in a potential-dependent fashion. This requires including another assumption into the analysis though: namely, the value of the Tafel slope.[16,70,71] Typical Tafel slopes are either 40 or 120 mV/dec, indicating that the second or the first elementary electrochemical step reveals the highest transition-state free energy, respectively. To illustrate this finding on a selected example, the OER over RuO_2(110) is adopted.[43,72] Figure 5 depicts the corresponding FED at applied overpotentials of 200 and 300 mV.

In Figure 5, the descriptor $G_{max}(\eta)$ is highlighted by a green arrow, and the free-energy diagram commences from the intermediate state with lowest free energy.[17,43,58,61,66] For η_{OER} = 0.20 V, the free-energy span governing $G_{max}(\eta)$ is reconciled with the transition from the O adsorbate to the formation of O_2 (M−O → M−OOH → M + O_2). In contrast, for η_{OER} = 0.30 V, the transition from the OOH adsorbate to the formation of O_2 (M−OOH → M + O_2) refers to the descriptor $G_{max}(\eta)$.

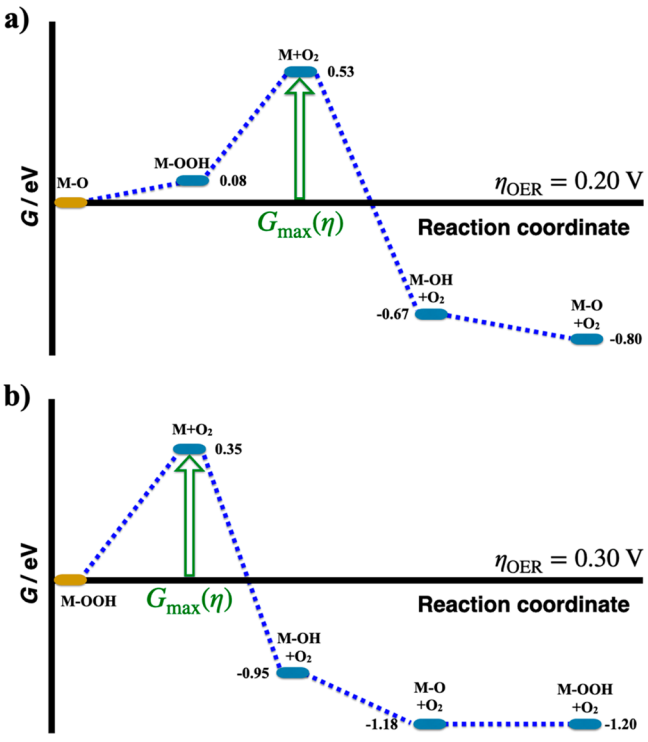

Figure 5. Free-energy diagram of the OER over RuO_2(110) at (a) η_{OER} = 0.20 V and (b) η_{OER} = 0.30 V. The descriptor $G_{max}(\eta)$ is given by the free-energy span from (a) M−O → M−OOH → M + O_2 or (b) M−OOH → M + O_2. These different free-energy spans have implications on the rate-determining step (RDS) dependent on the Tafel slope.

Let us assume that the Tafel slope amounts to 40 mV/dec at an applied overpotential of η_{OER} = 0.20 V. Hence, the second elementary electrochemical step refers to the decomposition of the OOH adsorbate, and thus, the step M−OOH → M + O_2 reveals the highest transition-state free energy and governs the OER rate. In contrast, if we assume a Tafel slope of 120 mV/dec, the formation of the OOH adsorbate, M−O → M−OOH, is rate determining. Similarly, for a Tafel slope of 120 mV/dec at η_{OER} = 0.30 V, the decomposition of the OOH adsorbate refers to the RDS. In principle, experimental studies of single-crystalline model electrodes allow extracting the precise potential-dependent value of the Tafel slope,[73,74] which can be merged with the concept of $G_{max}(\eta)$ to discuss the RDS. If experimental information on the Tafel slope remains unknown, it is yet possible to discuss the RDS in a qualitative fashion by referring to the standard values of 40 and 120 mV/dec, as outlined above. We use this methodology to discuss the nitrogen reduction reaction over transition-metal oxides in section 3.4 to compare the thermodynamic picture of the PDS with the RDS.

Finally, a short note on the compilation of free-energy diagrams and the discussion of the RDS is needed. As is evident from Figures 4 and 5, the free-energy landscapes commence from the RI with the smallest free energy, and this RI is not necessarily reconciled with the first step of the OER mechanism (cf. eq 1).[16,17] The reason for this finding is that only if the elementary steps commence from the RI with smallest free energy is the free-energy span model of $G_{max}(\eta)$ properly linked to the rate-determining states that refer to the RDS.[43,58] It should be noted that the renumbering procedure of the RIs in the free-energy diagram does not affect the numerical value of the descriptor $G_{max}(\eta)$, and thus, even without the renumbering procedure activity trends can be assessed in a predictive fashion. We refer to section 2 of the Supporting Information in ref 58, where this aspect is discussed in more detail. The renumbering procedure of the elementary steps is also discussed in several other works of the authors focusing on different electrocatalytic processes.[16,17,43,58,89,136,157]

2.5. Approximations Made within the Concept of $G_{max}(\eta)$. In sections 2.1−2.4, we have outlined the advantages of the descriptor $G_{max}(\eta)$ compared to the commonly applied notion of the thermodynamic overpotential, η_{TD}. Yet, it is also beneficial to point out the approximations made within the concept of $G_{max}(\eta)$.

First, the descriptor $G_{max}(\eta)$ relies on the assumption of a free-energy span model,[56,57] approximating electrocatalytic activity by the free-energy difference between the RIs with the smallest and highest free energy. The concept of a free-energy span model originates from the field of homogeneous catalysis, where often a single active site is encountered. This situation is fundamentally different from that of solid-state electrodes with a plethora of active sites adjacent to each other, and a critical parameter in this regard corresponds to the coverage of the RIs. It is therefore advisible to determine first the RI coverage such as by the construction of Pourbaix

https://doi.org/10.1021/acscatal.2c03997
ACS Catal. 2023, 13, 1740−1758

diagrams[25] before any claim on activity by means of the descriptor $G_{max}(\eta)$ is made. Otherwise, activity trends determined by the free-energy span model are prone to be erroneous.

Second, one may question whether a free-energy span is adequate to describe the activity of electrocatalytic processes occurring on solid-state electrodes. The notion of the free-energy span model relies on the assumption of quasi-equilibrium conditions,[68] whereas experimental measurements are commonly performed under steady-state conditions. Yet, the steady-state and quasi-equilibrium conditions often reveal identical results in terms of microkinetic modeling,[16] thus rendering the assumption of quasi-equilibrium conditions a viable approximation.

Finally, the descriptor $G_{max}(\eta)$ relies on a BEP relationship between the RI and TS with the highest free energy, quantified by the term $\Delta G^{\#}_{RDS\text{-}max}$ (cf. Figure 3). This BEP relation was determined by theoretical data from DFT calculations and experimental data from single-crystalline model electrodes for the RIs and TSs, respectively.[43] Further computational assessment of this BEP relation is desirable, which is, however, challenging due to the large errors of first-principles investigations on the kinetics in an electrochemical environment.[16,52] Of course, if deviations from the presumption that $\Delta G^{\#}_{RDS\text{-}max}$ is a constant with a sensitivity of 0.2 eV are observed, this would affect the predictive power of the free-energy span model relating to the notion of $G_{max}(\eta)$.

3. APPLICATION OF $G_{max}(\eta)$

3.1. Breaking Scaling Relation in the Oxygen Evolution Reaction. The OER plays a crucial role in proton-exchange-membrane (PEM) electrolyzers and metal–air batteries (MABs). The reaction kinetics of the OER is sluggish, which was related by Koper, Norskøv, Rossmeisl, and others to the binding energies of the RIs OH and OOH.[21,22] Koper argued that each ΔG_j value amounts to 1.23 eV for an ideal OER catalyst, giving rise to a thermoneutral FED at the OER equilibrium potential.[42,75] However, the binding energies of the OH and OOH adsorbates are inherently coupled, and the sum of the free-energy changes ΔG_2^{OER} and ΔG_3^{OER} is always larger than the anticipated theoretical value of 2 × 1.23 eV = 2.46 eV:

$$\Delta G_2^{OER} + \Delta G_3^{OER} = \text{SRI (scaling-relation intercept)} \tag{54}$$

The precise value of the scaling-relation intercept (SRI) may rely on the individual material class, the exchange-correlation functional employed in the DFT calculations, and the consideration or neglect of solvation.[48,76−79] An offset of 3.2 ± 0.20 eV is the most often reported SRI in the literature,[69] the value of which is within the functional independent SRI reported by Vegge and co-workers.[79] Therefore, breaking the SRI of about 3.2 eV to reach the optimum value of 2.46 eV, corresponding to a symmetrical thermodynamics FED, is considered a universal remedy to enhance OER activity.[80,81] Despite its popularity, this strategy is discussed controversially in the literature. According to the work of Calle-Vallejo and co-workers, breaking the scaling relation is a required yet not sufficient measure to ensure improved OER activity.[67,82] Application of the activity descriptor $G_{max}(\eta)$ provides further insight into the notion of breaking scaling relations. Figure 6a depicts an arbitrary thermodynamic FED for a scaling-relation-fulfilling catalyst (SRI = 3.2 eV) under typical OER conditions

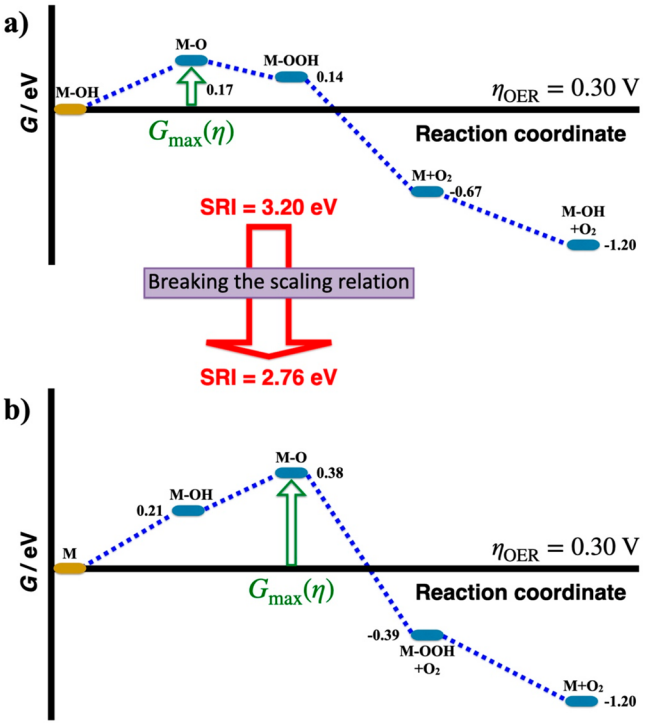

Figure 6. (a) Scaling-relation-fulfilling catalyst ($\Delta G_2^{OER} + \Delta G_3^{OER}$ = 3.2 eV) with ΔG_1^{OER} = 1.00 eV, ΔG_2^{OER} = 1.70 eV, ΔG_3^{OER} = 1.50 eV, and ΔG_4^{OER} = 0.72 eV. The activity descriptor $G_{max}(\eta)$ amounts to 0.17 eV under a typical OER condition: i.e., η = 0.3 V. (b) The OH vs OOH scaling relation is completely broken ($\Delta G_2^{OER} + \Delta G_3^{OER}$ = 2.46 eV), and the resulting free-energy penalty of 0.74 eV is completely assigned to the free-energy change ΔG_1^{OER}. The resulting scaling-relation-free catalyst reveals a lower electrocatalytic activity, quantified by $G_{max}(\eta)$ = 0.38 eV at η_{OER} = 0.3 V.

(η_{OER} = 0.3 V). The electrocatalytic activity of this catalyst can be evaluated by means of the descriptor $G_{max}(\eta)$, indicating $G_{max}(\eta = 0.3\ V) = 0.17$ eV.

It is a common practice to break the OH vs OOH scaling relation by reducing the free-energy change ΔG_3^{OER} until the desired SRI is reached. In this example, the resulting free-energy penalty of 0.74 eV is completely assigned to the free-energy change ΔG_1^{OER}. We obtain $G_{max}(\eta = 0.3\ V) = 0.38$ eV for the scaling-relation-free catalyst, indicating that, in this case, breaking the scaling relation is detrimental to obtaining higher OER activity.

Of course, a comment is needed on why the breaking of the OH vs OOH scaling relation may cause such an unfavorable scenario of lower activity. The main reason for this finding is traced to the fact that breaking the scaling relation relies on the notion that the PDS, as indicated by the descriptor η_{TD}, is also encountered with the RDS. If the free energy of the PDS is reduced, the electrocatalytic activity is enhanced due to the coupling of the thermodynamics to the kinetics via the BEP relation. As is evident from Figure 6, redistributing the free-energy changes to reach SRI = 2.46 eV has a major influence on the catalytic processes: the active site of the electrocatalyst (RI with the smallest free energy) and the free-energy span governing $G_{max}(\eta = 0.3\ V)$ are both altered. As such, the presumption PDS = RDS is violated when reducing ΔG_3^{OER} or any other free-energy change within the breaking of the OH vs OOH scaling relation to meet SRI = 2.46 eV, and this can be seen as the main reason this approach can have a disadvanta-

https://doi.org/10.1021/acscatal.2c03997
ACS Catal. 2023, 13, 1740−1758

geous effect on the optimization of electrocatalysts. The unsatisfactory picture relating to the breaking of the OH vs OOH scaling relation may raise the question of whether SRI = 2.46 eV is indeed encountered with the ideal situation in the OER. Recalling that the apex of the volcano plot is prone to change with increasing overpotential for a two-electron process,[83−86] a similar finding may also be encountered for the more complex four-electron OER.[50,87,88] With the support of another activity descriptor, the so-called electrochemical-step asymmetry index (ESAI),[60,66] it was demonstrated that the optimum thermodynamic FED in the OER switches from a symmetrical (thermoneutral) to an asymmetrical free-energy landscape (cf. Figure 7) as soon as the free-energy changes of

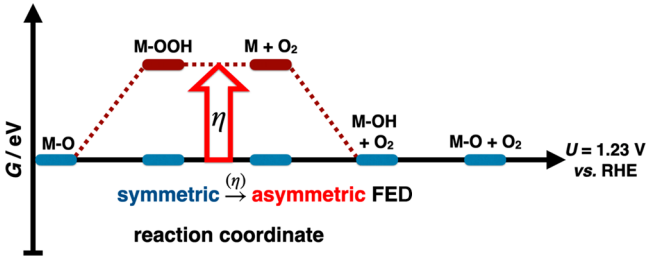

Figure 7. Comparison of the symmetrical and asymmetrical FED for the OER. In the symmetrical FED, all adsorbates are stabilized thermoneutrally at the OER equilibrium potential. This gives rise to the notion of 2.46 eV as the optimum SRI. On the other hand, for the asymmetric FED, the key adsorbate OOH is stabilized thermoneutrally at the target overpotential. For a target overpotential of 300 mV, the SRI of the asymmetric FED corresponds to 2.76 eV. It is argued that, upon increasing the overpotential, the optimum situation is encountered with the asymmetrical rather than with the symmetrical FED.

the mechanistic description are analyzed under the reaction conditions (η_{OER} > 0 V) rather than the equilibrium conditions. The SRI of the asymmetric thermodynamic free energy landscape, suggested as the thermodynamic ideal under operational conditions (η_{OER} > 0 V), depends on the amount of overpotential applied. For η_{OER} = 0.3 V, the asymmetrical thermodynamic FED reveals SRI = 2.76 eV.[60,61] While the notion of the asymmetric thermodynamic FED was introduced by a descriptor-based analysis in a qualitative fashion, a quantitative analysis is required to investigate whether breaking the scaling relation to SRI = 2.76 eV is accompanied by higher electrocatalytic activity than that to SRI = 2.46 eV.

We employed a data-driven methodology in combination with the descriptor $G_{max}(\eta)$ to account for the statistical significance of the symmetrical and asymmetrical thermodynamic FEDs.[89] For this purpose, we describe the available phase space of materials by a basis set in that we predefine the free-energy changes ΔG_1^{OER} and ΔG_2^{OER} as follows: ΔG_1^{OER} = ΔG_2^{OER} = [start = 0.00, stop = 2.50; step = 0.01] eV (the descriptions "start", "stop", and "step" are skipped throughout the rest of this perspective). This gives rise to about 63 000 cases in total. For all these cases, we start from the scaling-relation-fulfilling catalyst (SRI = 3.2 eV) and analyze the energetics at different electrode potentials, U = [1.33, 1.43, 1.53] V vs RHE, corresponding to OER overpotentials of η_{OER} = (100, 200, 300) mV, respectively. For all data points, $G_{max}(\eta)$ is calculated by eq 25. In the next step, we alter the SRI to 2.46 or 2.76 eV corresponding to the thermodynamic symmetrical or asymmetrical FED, respectively. This is achieved by reducing the value of ΔG_3^{OER} to meet an SRI of 2.46 or 2.76 eV, and the corresponding energy penalty is reassigned to the free-energy change ΔG_4^{OER} so that the OER equilibrium condition is not violated. For the symmetrical and asymmetrical free energy landscape, the electrocatalytic activity is quantified by the descriptor $G_{max}(\eta)$, and the obtained $G_{max}(\eta)$ values dependent on the applied electrode potential are compared to the scaling-relation-fulfilling catalysts (SRI = 3.2 eV). We evaluated the percentage of cases for which the electrocatalytic activity of the asymmetrical or symmetrical FED is equal to or higher than that of the scaling-relation-fulfilling catalysts. Consequently, the conditions of eq 55 or 56 need to be fulfilled:

$$G_{max}(\eta)@(\mathrm{SRI} = 2.46\ \mathrm{eV}) \leq G_{max}(\eta)@(\mathrm{SRI} = 3.2\ \mathrm{eV}) \quad (55)$$

$$G_{max}(\eta)@(\mathrm{SRI} = 2.76\ \mathrm{eV}) \leq G_{max}(\eta)@(\mathrm{SRI} = 3.2\ \mathrm{eV}) \quad (56)$$

The results of our statistical analyses are summarized in Table 1.

Table 1. Breaking the SRI from 3.2 eV to 2.76 (Asymmetrical FED) or 2.46 eV (Symmetrical FED) at Different Overpotentials[a]

η/V	breaking scaling relation	equal or higher activity (%)
0.1	SRI = 3.2 eV → SRI = 2.46 eV	90.6
0.1	SRI = 3.2 eV → SRI = 2.76 eV	100
0.2	SRI = 3.2 eV → SRI = 2.46 eV	89.1
0.2	SRI = 3.2 eV → SRI = 2.76 eV	96.0
0.3	SRI = 3.2 eV → SRI = 2.46 eV	88.0
0.3	SRI = 3.2 eV → SRI = 2.76 eV	95.0

[a]The last column indicates the percentage of electrocatalysts based on our chosen basis set that reveal equal or higher activity in the approximation of $G_{max}(\eta)$ (cf. eqs 55 and 56).

It is evident from Table 1 that breaking the scaling relation from 3.2 to 2.76 eV (asymmetrical FED) yields higher or equal activity in more cases than breaking the scaling relation from SRI = 3.2 eV to SRI = 2.46 eV (symmetrical free energy landscape), independent of the amount of overpotential applied. Surprisingly, the impact of breaking the scaling relation is potential dependent and turns out to be beneficial at small rather than large overpotentials. One may argue that this finding may be related to the fact that formation of the OOH adsorbate, corresponding to the free-energy change ΔG_3^{OER}, is rate determining for small overpotentials.[44,59,82,90,91] However, for overpotentials exceeding 300 mV, also decomposition of the OOH adsorbate can be reconciled with the RDS, and this step as the RDS does not have a positive impact on the breaking of the OH vs OOH scaling relation.[17,92−94]

In summary, the activity descriptor $G_{max}(\eta)$ contributed to extend our understanding of breaking the scaling relation in the OER. Our analysis reveals that SRI = 2.76 eV is statistically more significant than SRI = 2.46 eV to reach higher electrocatalytic activity, suggesting a change in the mindset when thermodynamic concepts are applied for catalyst optimization.

3.2. Bifunctional Oxygen Electrocatalysis. The data-science approach presented in section 3.1 for the OER was also exerted to investigate the bifunctional oxygen electrocatalysis

https://doi.org/10.1021/acscatal.2c03997
ACS Catal. 2023, 13, 1740−1758

at the cathode of MABs. This type of battery is discussed as a potential replacement for lithium-ion batteries (LIBs) due to its higher energy density than that of LIBs.[7−9,95,96] However, the performance of MABs is restrained by the four-electron ORR and OER taking place during discharge and charge of the device, respectively. While the mechanistic description of the OER has been discussed beforehand (cf. eqs 1−4), the elementary steps of the ORR are given by eqs 57−60:[97−100]

$$O_2 + M + H^+ + e^- \rightarrow M{-}OOH \qquad \Delta G_1^{ORR} \qquad (57)$$

$$M{-}OOH + H^+ + e^- \rightarrow H_2O_{(l)} + M{-}O \qquad \Delta G_2^{ORR} \qquad (58)$$

$$M{-}O + H^+ + e^- \rightarrow M{-}OH \qquad \Delta G_3^{ORR} \qquad (59)$$

$$M{-}OH + H^+ + e^- \rightarrow M + H_2O_{(l)} \qquad \Delta G_4^{ORR} \qquad (60)$$

These four energy changes sum up to −4.92 eV at U = 0 V vs RHE:

$$\Delta G_1^{ORR} + \Delta G_2^{ORR} + \Delta G_3^{ORR} + \Delta G_4^{ORR} = -4.92\ \text{eV} \qquad (61)$$

Similar to eq 54, the inherent coupling of the OH and OOH adsorbates yields

$$-\Delta G_2^{ORR} - \Delta G_3^{ORR} = \text{SRI} \qquad (62)$$

For optimum performance, a highly active bifunctional electrocatalyst that catalyzes both the OER and ORR at low overpotentials with a reasonable current density is required.[101−103] Experimentally, the performance of bifunctional materials is assessed by the so-called bifunctional index (BI) (cf. Figure 8), defined as[103]

$$\text{BI} = U\left(@j_{OER} = 10\frac{\text{mA}}{\text{cm}^2}\right) - U\left(@j_{ORR} = -1\frac{\text{mA}}{\text{cm}^2}\right) \qquad (63)$$

Please note that up to three different definitions for the reduction process (ORR) can be found in the literature. Besides the electrode potential to reach j_{ORR} = −1 mA/cm^2, also j_{ORR} = −3 mA/cm^2 or the half-wave potential (HWP) is reconciled with performance measures to characterize electrode materials in the ORR.[104,105] In the remainder of this discussion, j_{ORR} = −1 mA/cm^2 is used. While the BI can be determined by experimental cyclic voltammetry, we emphasize that in previous theoretical studies the BI was approximated by the sum of the thermodynamic overpotentials, η_{TD}, for the OER and ORR:[67,106]

$$\text{BI} \approx \eta_{TD}^{OER} + \eta_{TD}^{ORR} \qquad (64)$$

While in a homologous series of materials η_{TD} may scale with the current density to reach 10 mA/cm^2, it is evident that the cathodic ORR process cannot be captured by this simple descriptor (cf. eq 63). Consequently, application of the formula in eq 64 would result in BI values that always exceed the experimentally measured values. Given that the application of the descriptor $G_{max}(\eta)$ allows an approximation of current densities by microkinetic modeling (see section 2.3), we make use of this feature to put forth a method of how to determine the BI from a dedicated analysis of adsorption free energies in conjunction with data-science techniques. Our procedure is similar to that reported in the previous section in that we set up a basis set that may describe the phase space of available materials. Identically with the investigation of breaking the scaling relation,[89] our basis set is defined by $\Delta G_1^{OER} = \Delta G_2^{OER}$ = [0.00, 2.50; 0.01] eV and $\Delta G_4^{ORR} = \Delta G_3^{ORR}$ = [−2.50, 0.00; 0.01] eV. Knowledge of $\Delta G_2^{OER}/\Delta G_3^{ORR}$ enables determination of $\Delta G_3^{OER}/\Delta G_2^{ORR}$ by referring to the SRI (cf. eqs 54 and 62), for which we choose an array of [2.90, 3.20; 0.10] eV for the OER and ORR. These values are selected based on the reported SRIs in the literature.[48,50,69,76,107−109] Consequently, $\Delta G_4^{OER}/\Delta G_1^{ORR}$ can be directly obtained from the equilibrium condition (cf. eqs 8 and 61 for the OER and ORR, respectively), and $G_{max}(\eta)$ can be determined for all cases by eq 25.

In the next step, $G_{max}(\eta)$ is used to determine the current density as a function of the applied electrode potential (cf. eq 53). This requires the definition of additional input parameters: namely, the density of active surface sites, Γ_{act}, and the constant that connects the descriptor $G_{max}(\eta)$ to the rate-determining transition state. We choose Γ_{act} = [10^{14}, 5 × 10^{14}, 10^{15}] cm^{-2} and const = [0.4, 0.5, 0.6] eV in the analysis. For a rough screening of the parameter space, we use applied electrode potentials of U = [1.13, 1.03, 0.93] V vs RHE and [1.33, 1.43, 1.53 V] vs RHE for the ORR and OER, respectively, corresponding to applied overpotentials of η = (±100, ±200, ±300) mV, to calculate j_{OER} and j_{ORR}. All of these values are stored in a multidimensional database consisting of more than 13.6 million data points (cf. Figure 9).

The database of Figure 9 is the starting point to derive the BI for our basis set and to compare the obtained BI values with experiments. While the concrete statistical treatment is described in detail in ref 64, we want to focus on the main conclusions that can be rendered based on the application of $G_{max}(\eta)$. Our study aims to identify highly active bifunctional catalysts, and we have extracted those from our database and compared them to experiments (cf. Figure 10). While previous theoretical studies on the BI in the approximation of the thermodynamic overpotential reported that theoretical BI values are in good agreement with the experimental values,[106] our statistical approach clearly demonstrates that there is still plenty of room for improvement for the performance of bifunctional materials in the oxygen electrocatalysis. This statement holds true despite scaling relations, and even for the most common SRI of 3.2 eV an amelioration of at least 0.1 V

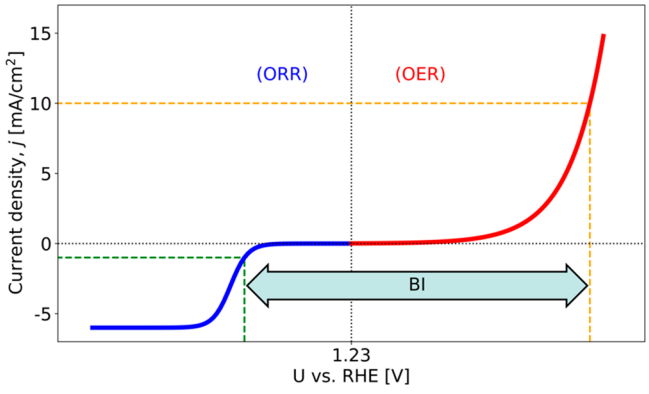

Figure 8. Current density, j, vs applied electrode potential, U, for the oxygen electrocatalysis, consisting of the OER (red) and ORR (blue), as obtained from cyclic voltammetry experiments. The bifunctional performance of electrocatalysts in the oxygen electrocatalysis can be assessed by the difference in electrode potential between j_{OER} = 10 mA/cm^2 and j_{ORR} = −1 mA/cm^2, denoted BI. Reproduced with permission from ref 64.

https://doi.org/10.1021/acscatal.2c03997
ACS Catal. 2023, 13, 1740−1758

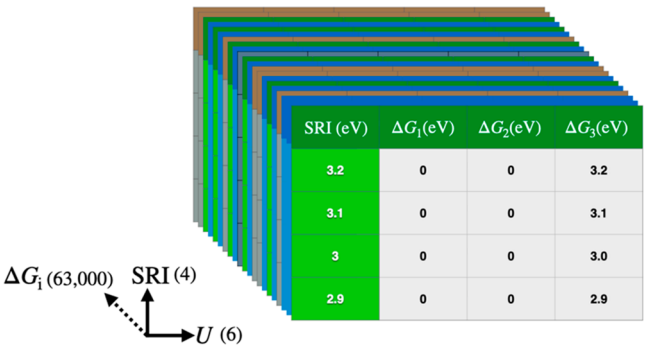

Figure 9. Schematic illustration of our multidimensional database, consisting of more than 13 million data points, to determine the BI in the oxygen electrocatalysis for any hypothetical electrode material from theory. $\Delta G_j^{OER/ORR}$, SRI, and U denote the adsorption free energies, scaling-relation intercept, and applied electrode potential, respectively. Behind these variables, their respective number of cases is given in parentheses. Reproduced with permission from ref 64.

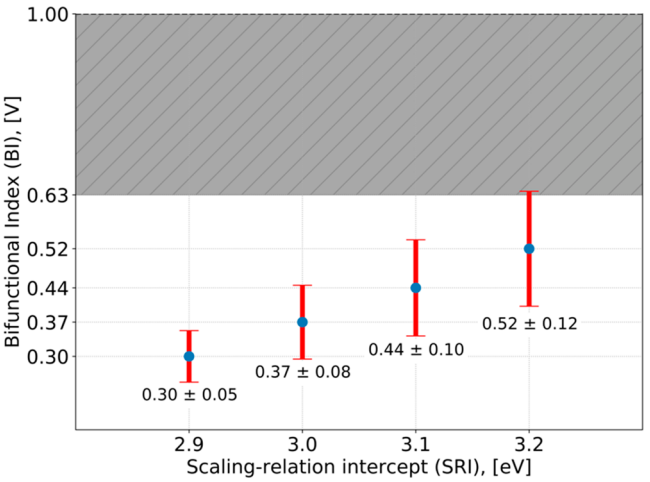

Figure 10. Average BI (blue dots) accompanied by their standard deviation dependent on the SRI, as obtained from our data-driven model for highly active bifunctional OER/ORR catalysts. The shaded region indicates the experimentally reported BIs of highly active bifunctional materials. Reproduced with permission from ref 64.

relating to the BI appears feasible. Yet, a comment is needed how the deviation from our theoretical predictions to the experimental BI values is interpreted.[110]

In our model, we assume that the adsorption free energies in the potential range of the OER (U > 1.23 V vs RHE) as well as the ORR (U < 1.23 V vs RHE) are the same. Thus, it is tacitly presumed that the active sites in the OER and ORR are identical, a supposition that may not always be fulfilled. Consequently, for experimentally synthesized materials the adsorption free energies in the OER regime may differ from the adsorption free energies in the ORR because the morphology of the electrode surface is prone to change when the applied electrode potential is altered. This finding suggests that, for experimentally synthesized materials, the set of adsorption free energies is optimized for only one process within the oxygen electrocatalysis, whereas the set of adsorption free energies is not fully optimized for the reverse reaction. It would therefore be required to design bifunctional electrocatalysts with two different active sites in that the first active site reveals an optimized set of $\Delta G_{j=1,2,3,4}^{OER}$ values in the potential range of U > 1.23 V vs RHE, while the second active site should have an optimized set of $\Delta G_{j=1,2,3,4}^{ORR}$ values in the potential range of U < 1.23 V vs RHE. For an example of a bifunctional catalyst with two different active sites, the reader is referred to ref 110.

We conclude that the application of $G_{max}(\eta)$ in conjunction with data-science techniques may contribute to bridging the gap between *ab initio* theory and experiments by providing advanced insight into the performance of bifunctional electrocatalysts for the oxygen electrocatalysis beyond the approximation of the thermodynamic overpotential. Further theoretical studies are needed to comprehend implications for efficient bifunctional oxygen electrocatalysis on the atomic scale and to determine how the prediction of BI values by $G_{max}(\eta)$ is related to the proposed limit of BI = 0.74 V based on scaling relations.[106]

3.3. Oxygen Evolution vs Peroxide Formation: Application of $G_{max}(\eta)$ to a Selectivity Problem.

H_2O_2 (hydrogen peroxide) is an important industrial chemical: e.g., for water disinfection. While so far H_2O_2 is mainly produced by the anthraquinone process containing of hazardous materials, the electrochemical oxidation of water is an alternate, sustainable pathway to generate H_2O_2. Yet, the two-electron oxidation of water to H_2O_2, also denoted as the peroxide formation reaction (PFR), is thermodynamically restrained because of its equilibrium potential of 1.76 V vs RHE, which is about 500 mV higher than that of the four-electron OER. Despite this, the PFR is kinetically preferred because it requires fewer electron transfers than the OER. Ultimately, the production of H_2O_2 by electrolysis requires overcoming the selectivity challenge of the competing OER and PFR. Consequently, an electrode material with high affinity toward the PFR, which at the same time efficiently suppresses the OER, is needed. Previous theoretical studies in the DFT approximation used the descriptor η_{TD} to compile volcano curves at the equilibrium potential of the PFR.[111−114] Quite in contrast, the descriptor $G_{max}(\eta)$ allows studying the selectivity problem of the competing reaction channels in a potential-dependent fashion, as outlined in the following.

The reaction mechanism of the PFR is given by eqs 65 and 66:

$$M + H_2O_{(l)} \rightarrow M{-}OH + H^+ + e^- \quad (65)$$

$$M{-}OH + H_2O_{(l)} \rightarrow M + H_2O_{2(l)} + H^+ + e^- \quad (66)$$

In comparison to the OER, the PFR shares a common intermediate (*OH) with this pathway, but in the second proton−electron transfer step, the OH adsorbate is directly converted into H_2O_2. Consequently, an active PFR catalyst may not be prone to oxidize and thus may not bind the O adsorbate strongly because this may indicate a tendency to catalyze the OER rather than the PFR. In the literature, carbon-based materials, such as boron-doped diamond (BDD), have been discussed as anode materials for the electrocatalytic production of H_2O_2.[115−117]

We modeled BDD in a first-order approximation as a single-atom-thin layer of graphite in the [001] direction because BDD can be reconciled with a partially graphitized diamond surface.[118,119] Various slab models with different adsorbate densities were optimized. Altogether, eight coverage densities were studied, and the models containing adsorbate densities of 3−12.5% and 17−25% correspond to the low- and high-coverage compositions, respectively. Models are labeled G*N*,

https://doi.org/10.1021/acscatal.2c03997
ACS Catal. 2023, 13, 1740−1758

where N is the number of carbon atoms per supercell, while the coverage density is equal to $1/N$. Two of these structures are schematically shown in Figure 11. The G6 and G16 models correspond to coverage densities of 17% and 6%, respectively, thus representing high and low adsorbate densities.

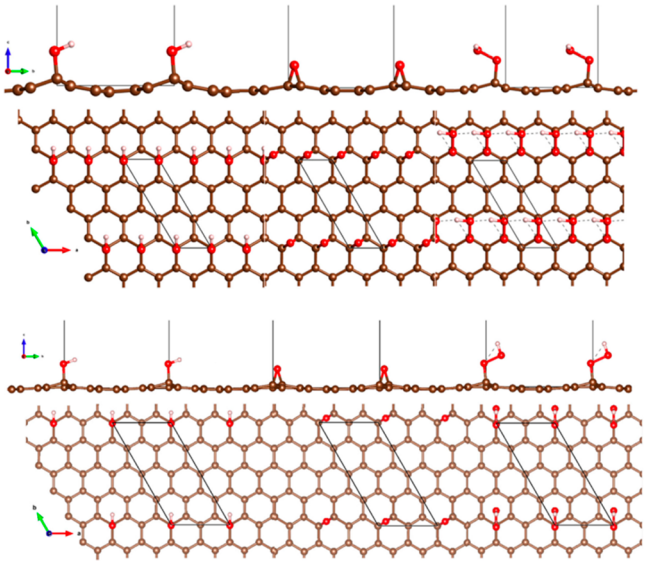

Figure 11. Example of the optimized geometry for the G6 model with high coverage (top) and the G16 model with low coverage (bottom) for the OH, O, and OOH adsorbates (from the left to the right). Unit cells are shown by solid lines. Both coverage concentrations are presented in two different projections. Reproduced with permission from ref 120.

For the low- and high-coverage compositions, we compiled FEDs of our BDD model for the OER and PFR at the PFR equilibrium potential (cf. Figure 12). The free-energy diagrams allow determining the descriptor $G_{max}(\eta = 0\ V)$ for the OER and PFR, using the free-energy span model from the RI with the lowest free energy to the RI with highest free energy, as introduced in section 2. For an accurate determination of the PFR free-energy landscape, gas-phase error corrections are called for, as discussed by Calle-Vallejo and co-workers.[121] In the presented approach, we make use of the experimental equilibrium potential rather than calculate the H_2O_2 molecule because the latter may result in an inaccurate equilibrium potential for the PFR.

Our analysis shows that, for the 2e$^-$ PFR, the free-energy span associated with $G_{max}(\eta)$ refers to the formation of the OH adsorbate with G_{max}^{PFR} in a range of 0.90−1.08 eV. Moreover, for the 4e$^-$ OER, the transition from the O adsorbate to the OH intermediate is thermodynamically the most uphill in the free energy landscape with G_{max}^{OER} in a range of 1.34−1.52 eV. This finding demonstrates that at U = 1.76 V vs RHE the selectivity should be in favor of peroxide formation due to the lower thermodynamic restraints, resulting in superior kinetics according to the BEP relation.[28,122−124]

While the free-energy span associated with the descriptor G_{max}^{PFR} is related to $G_{M-OH} - G_M$, the most stable surface termination corresponds to M−O or M−OOH for high and low coverages, respectively (cf. Figure 12). Accordingly, one may claim that the M−O or M−OOH surface compositions first need to be converted into M so that the PFR can occur. The transition of M−O or M−OOH to M may add a free-energy penalty to the descriptor G_{max}^{PFR}, which affects the selectivity analyses. Given that the coverage density does not exceed 25% (cf. Figure 11), there are M−O, M−OOH, and M surface sites available, and the first two surface sites facilitate the OER whereas the latter is the starting point for the PFR. However, we emphasize that, in the case of higher coverages, it is important to consider the poisoning effects of adsorbates that can be incorporated by means of a free-energy penalty into the free-energy span model of $G_{max}(\eta)$.

It might be interesting to indicate that the descriptor G_{max}^{PFR}, evaluated at zero overpotential, is identical with the thermodynamic overpotential because the PFR is a two-electron process consisting of only one intermediate. The difference between the free-energy span approach and η_{TD} manifests as soon as the analysis is conducted in a potential-dependent fashion, as discussed in the following.

The evaluation of G_{max}^{PFR} and G_{max}^{OER} as a function of applied PFR overpotential is indicated by $G_{max}^{PFR}(\eta)$ and $G_{max}^{OER}(\eta)$, respectively. The difference between these two descriptors, $G_{sel}(\eta)$, at a fixed electrode potential is a benchmark for PFR selectivity dependent on the driving force:

$$G_{sel}(\eta) = G_{max}^{OER}(\eta) - G_{max}^{PFR}(\eta) \tag{67}$$

Following the selectivity model of Exner for the competing chlorine and oxygen evolution reactions,[122,125] an expression for the potential-dependent PFR selectivity can be derived taking the Butler−Volmer formalism into account:

$$\text{PFR sel}\ (\eta) = \frac{\exp\left(\frac{G_{sel}(\eta)}{k_B T}\right)}{\exp\left(\frac{G_{sel}(\eta)}{k_B T}\right) + 1} \tag{68}$$

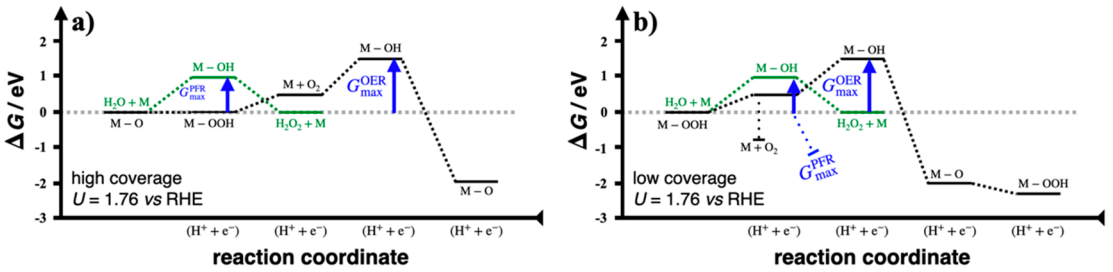

Figure 12. FEDs of 2e$^-$ PFR (green), and 4e$^-$ OER (black) at the PFR equilibrium (U = 1.76 V vs RHE, pH = 0), generalized for graphene-like surfaces by averaging the values of ΔG for models with high and low coverage. The descriptors $G_{max}^{PFR}(\eta = 0)$ and $G_{max}^{OER}(\eta = 0)$, defining the thermodynamic penalty to move from the RI with the lowest free energy to the RI with the highest free energy for the PFR and OER, respectively, are indicated by blue arrows. Figure adopted with changes from ref 120.

https://doi.org/10.1021/acscatal.2c03997
ACS Catal. 2023, 13, 1740−1758

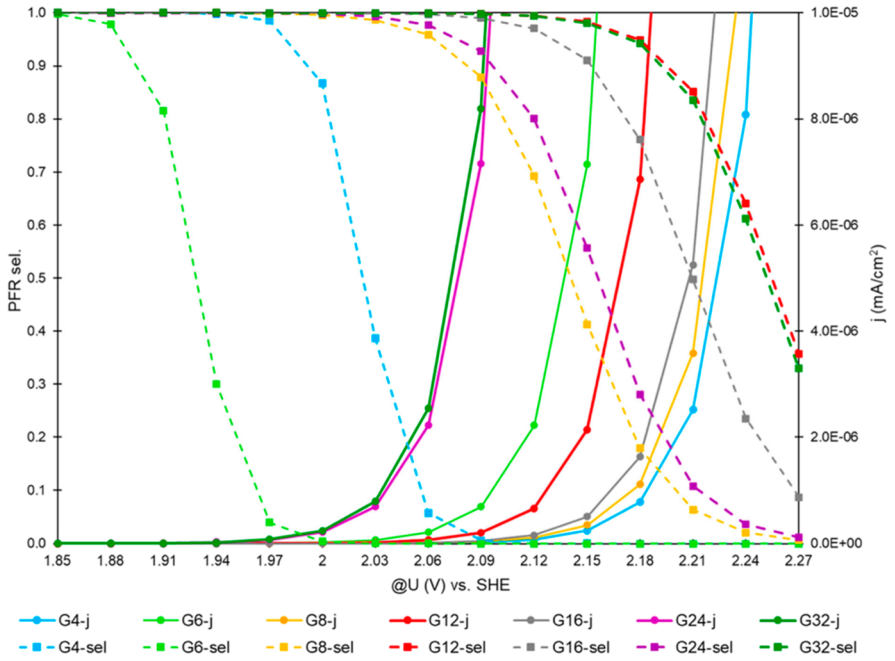

Figure 13. PFR selectivity and theoretically calculated PFR current densities as a function of the applied bias (@U vs SHE @pH = 0) for all graphene models (G4, 25%; G6, 17%; G8, 12.5%; G12, 8.3%; G16, 6%; G24, 4%; G32, 3%), in which the coverage densities are indicated in percentages. Current densities are calculated by referring to the formalism introduced in section 2.3. Reproduced with permission from ref 120.

In eq 68, k_B denotes the Boltzmann constant and T amounts to 298.15 K. PFR sel (η) can adopt values between 0 and 1, denoting 100% selectivity for the OER or 100% selectivity for the PFR, respectively. Evaluating $G_{max}^{PFR}(\eta)$ and $G_{max}^{OER}(\eta)$ to calculate $G_{sel}(\eta)$ and PFR sel (η) has the following advantages: (i) PFR selectivity can be discussed as a function of the applied electrode potential because PFR selectivity may change upon modifying the driving force and (ii) current densities for the PFR can be approximated using the formalism introduced in section 2.3. Knowledge of current densities enables assessing, at least in a qualitative fashion, whether the produced amount of H_2O_2 per time is sufficient for experimental applications. These results are summarized in Figure 13. For the high-coverage regime (17−25%), the BDD model maintains a large PFR selectivity up to 100% up to U = 2 V vs RHE, whereas for U > 2 V vs RHE, PFR selectivity deteriorates. In contrast, for the low-coverage regime (3−12.5%), PFR is the dominant reaction for U < 2.11 V vs RHE, but for higher electrode potentials the OER is superior to the PFR. Reference 126 highlighted an inverse correlation between the current density and the selectivity toward H_2O_2; hence, a condition for low working overpotentials inherently implies low current densities. Our investigation underpins this inverse relation where the highest current density of about 10^{-5} mA/cm^2 is achieved for the lowest adsorbate concentrations (3% and 4%) @U = (2.05−2.10) V vs SHE (@pH = 0). The optimum adsorbate density is below 8% coverage because these surface compositions can achieve current densities above 10^{-6} mA/cm^2 while maintaining reasonable PFR selectivity.

Applying the concept of $G_{max}(\eta)$ to the selectivity problem of the OER and PFR enabled us also to gain further insight compared to the notion of η_{TD}. The analysis of the FEDs in Figure 12 illustrates that the relation $\eta_{TD}^{OER} = \eta_{TD}^{PFR}$ is met at U = 1.76 V vs RHE, resulting in the conclusion that the PFR selectivity is 50% irrespective of the coverage. Since the thermodynamic overpotential does not account for the effect of the applied overpotential on the energetics, PFR selectivity in the approximation of η_{TD} is also independent of the driving force and remains 50% when increasing the applied overpotential is increased. Additionally, approximating electrocatalytic activity and selectivity by η_{TD} does not allow predicting current densities in contrast to the approach of $G_{max}(\eta)$. Given that the PFR selectivity is a strong function of coverage and the applied overpotential according to experimental investigations,[117] we conclude that the application of $G_{max}(\eta)$ to a selectivity problem is a significant improvement compared to the use of η_{TD}, thus opening new doors in the understanding of competing reaction channels.

3.4. Kinetic Volcano Plots for the Nitrogen Reduction Reaction over Transition-Metal Oxides. Ammonia (NH_3), an important precursor to produce fertilizers, dyes, and medicaments, is mainly manufactured by the traditional Haber−Bosch process.[127−129] Unfortunately, this process is environmentally unfriendly because it releases 450 million tons of CO_2 per annum, corresponding to more than 1% of the global carbon dioxide emissions.[130] A promising sustainable route refers to electrochemical ammonia synthesis. However, the major hurdle in this regard is the competing HER, which takes place in the same potential window as the nitrogen reduction reaction (NRR).[131,132] Besides, the NRR requires larger overpotentials than the HER because six electrons are transferred in the overall reaction to produce one molecule of ammonia (cf. eq 69), whereas the HER is a facile two-electron process (cf. eq 69):

$$N_2 + 6H^+ + 6e^- \rightarrow 2NH_3 \quad U_{NRR}^0 = 0.148 \text{ vs RHE} \quad (69)$$

$$2H^+ + 2e^- \rightarrow H_2 \quad U_{HER}^0 = 0 \text{ vs RHE} \quad (70)$$

Previous theoretical studies on the NRR have focused on the concept of η_{TD} in combination with the construction of volcano plots to determine the PDS that may limit the overall

https://doi.org/10.1021/acscatal.2c03997
ACS Catal. 2023, 13, 1740−1758

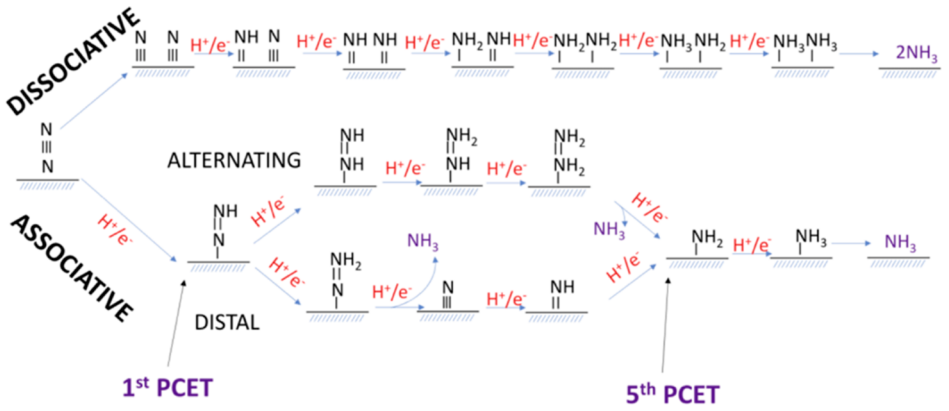

Figure 14. Schematic representation of the associative and dissociative NRR mechanisms. Reproduced with permission from ref 136.

reaction in the thermodynamic picture. Volcano curves can be constructed for the proposed mechanistic descriptions of the NRR that range from a dissociative pathway to an associative mechanism (cf. Figure 14). Given that breaking the N−N triple bond is energetically demanding, most electrode materials may follow the associative pathway, and in the following we are focusing on the volcano plot for this mechanistic description. While the associative mechanism can be differentiated into alternating and distal pathways, the volcano plots of Skúlason and co-workers for metals, transition-metal oxides, and other material classes indicate that the PDS is encountered with either the first reaction step (formation of the NNH adsorbate) or the last reaction step (formation of NH_3 out of the NH_2 adsorbate).[55,133−136] Both the alternating and distal mechanisms have these steps in common, so that the precise nature of the electrochemical protonation steps between the first and last reaction steps were thought not to be of the highest importance for materials development. A schematic overview of the thermodynamic volcano, where the formation of ammonia or the formation of the NNH adsorbate is limiting at the left or right volcano legs, respectively, is given in Figure 15.

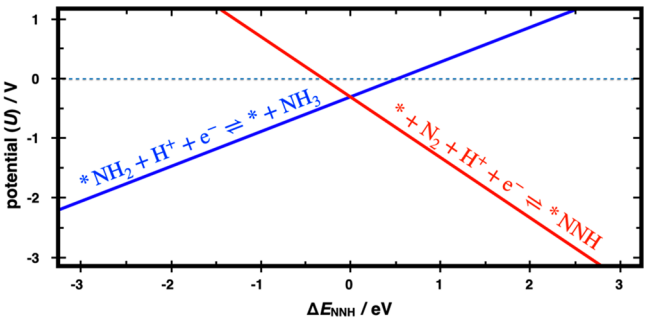

Figure 15. Schematic illustration of the volcano plot for the NRR over transition-metal oxides. The formation of ammonia (blue) or the formation of the NNH adsorbate (red) is reconciled with the limiting reaction steps in the thermodynamic picture at the left and right volcano legs, respectively. Figure adopted with changes from ref 134.

In the following, we apply the descriptor $G_{max}(\eta)$ to factor overpotential and kinetic effects into the analysis of trends in the NRR, thereby aiming to resolve the RDS as introduced in section 2.4. In this context, we refer to the material class of transition-metal oxides which follows the conventional scheme of NNH or NH_3 formation as the PDS at the right and left volcano legs.[134,135] While we want to refrain from a long mathematical derivation, the respective details of how to apply $G_{max}(\eta)$ to the NRR can be found in a recent article.[136] Also, we want to point out the importance of gas-phase error corrections for the energetic description of the NRR, because without these mandatory corrections, inaccurate or even erroneous equilibrium potentials, free-energy changes, and activity predictions are observed.[137] Starting with the associative distal mechanism, which comprises the *NNH, *NNH_2, *N, *NH, and *NH_2 adsorbates (cf. Figure 14), we extract the largest free-energy span corresponding to the descriptor $G_{max}(\eta)$ at an applied electrode potential of U = −0.2 V vs RHE by varying the descriptor ΔG_1, which corresponds to the adsorption free energy of the NNH adsorbate, between −2.5 and +2.5 eV. The electrode potential of U = −0.2 V was chosen because it may refer to the conditions in experimental studies.[138] The result of this investigation is shown in Figure 16, indicating that different free-energy spans may limit the rate dependent on ΔG_1. Most notably, it becomes evident that a combination of several elementary reaction steps rather than a single reaction step is energetically most uphill in free energy at the right volcano leg (cf. Figure 16a), a feature than cannot be resolved by means of η_{TD}.

In the next step, we use the largest free-energy span based on the descriptor $G_{max}(\eta)$ to determine the RDS. In this context, we assume a Tafel slope of 120 mV/dec, which assigns the first elementary reaction step to be rate limiting. This assumption is corroborated by the fact that the cathodic potential regime of U = −0.2 V vs RHE corresponds to an applied overpotential of about 350 mV when referring to the standard equilibrium potential, and for these overpotential regimes typically the first step may be the limiting one. On the left side of the volcano, the elementary step *NH_2 → NH_3 is reconciled with the largest free-energy span governing $G_{max}(U$ = −0.20 V vs RHE). Consequently, the RDS is the transition from *NH_2 to NH_3, since this is the first elementary step in the reaction sequence. A different situation, however, is encountered close to or at the volcano apex. There, the sequences of steps *NNH → *NNH_2 or *NNH → *NNH_2 → *N → *NH are related to the $G_{max}(U$ = −0.20 V vs RHE) span. Since b = 120 mV/dec purports the first elementary step to be rate limiting, for both regions *NNH → *NNH_2 is identified as the RDS. In the same fashion, N_2 → *NNH is obtained as the RDS at the right leg of the volcano for the $G_{max}(U$ = −0.20 V vs RHE) spans of N_2 → *NNH → *NNH_2 → *N → *NH and N_2 → *NNH →

https://doi.org/10.1021/acscatal.2c03997
ACS Catal. 2023, 13, 1740−1758

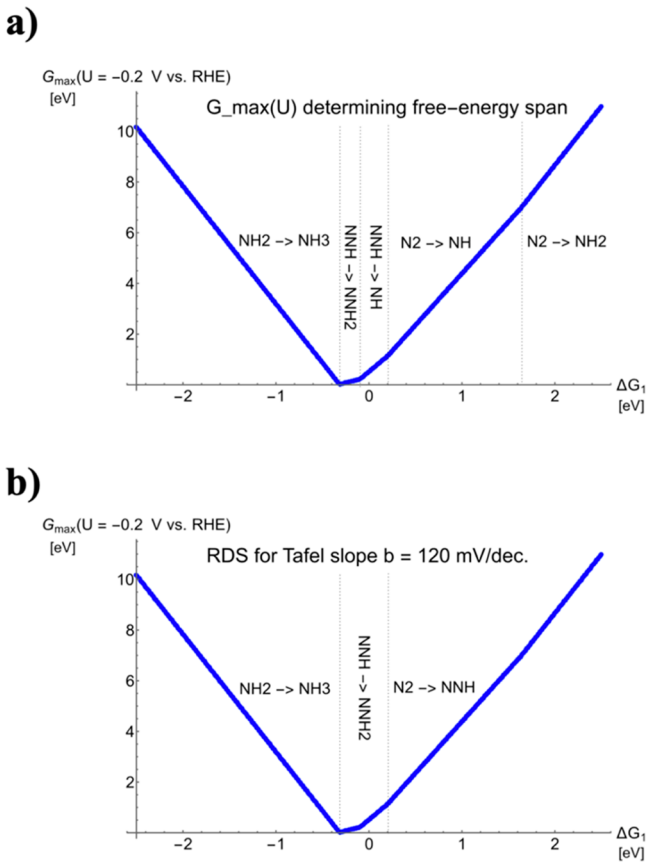

Figure 16. (a) Volcano plot for the NRR over transition-metal oxides according to the associative distal mechanism. (b) RDS derived at U = −0.2 V vs RHE based on the concept of $G_{max}(\eta)$, which goes beyond the common volcano interpretation in terms of the PDS (cf. Figure 14). Reproduced with permission from ref 136.

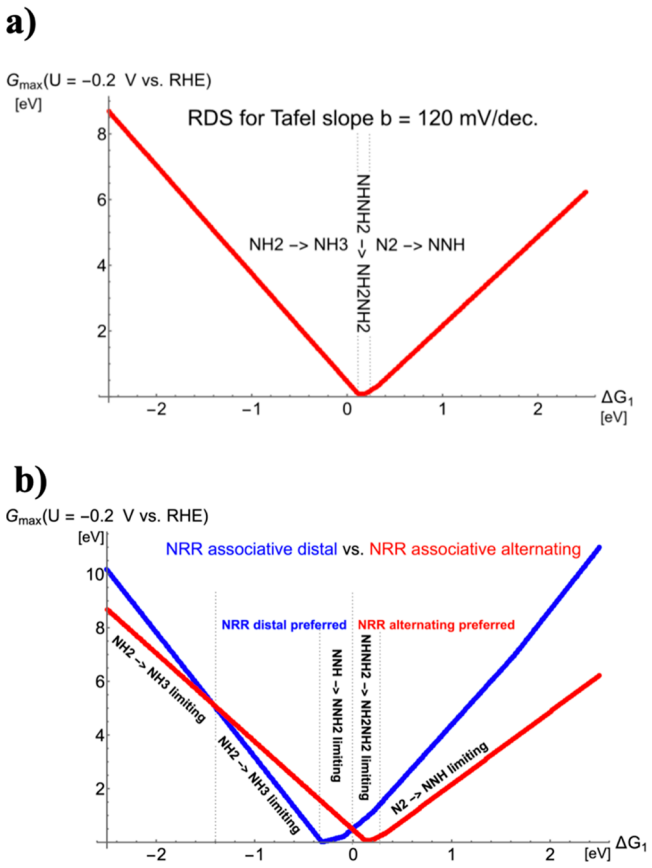

Figure 17. (a) Volcano plot for the NRR over transition-metal oxides according to the associative alternating mechanism, following the same procedure as for the associative distal mechanism in Figure 15. The rate-determining step (RDS) is determined for a Tafel slope of b = 120 mV/dec at U = −0.2 V vs RHE based on the concept of $G_{max}(\eta)$, which goes beyond the thermodynamic information in terms of the potential-determining step (cf. Figure 15). (b) Comparison of the associative distal (blue) and associative alternating (red) mechanisms to elucidate the preferred mechanistic description and limiting reaction steps. Reproduced with permission from ref 136.

$^*NNH_2 \rightarrow {}^*N \rightarrow {}^*NH \rightarrow {}^*NH_2$. The kinetic volcano plot indicating the RDS for the associative distal mechanism is depicted in Figure 16b.

In the same fashion as for the associative alternating mechanism, we apply the concept of $G_{max}(\eta)$ to the associative distal pathway, which consists of the *NNH, *NHNH, $^*NHNH_2$, $^*NH_2NH_2$, and $^*NH_2$ adsorbates (cf. Figure 14). Using the same reasoning and approximations, we resolve the RDS for this pathway (cf. Figure 17a). Similar to the associative alternating mechanism, it turns out that the correlation RDS = PDS is fulfilled at the volcano legs for the associative distal pathway because formation of either NH_3 or the *NNH adsorbate limits the rate at the left and right volcano legs, respectively. However, at the volcano apex, a surface reaction, namely the step $^*NHNH_2 \rightarrow {}^*NH_2NH_2$, governs the reaction kinetics at U = −0.2 V vs. RHE.

The volcano plots for the associative alternating and distal mechanisms are combined to identify which mechanism is preferred, dependent on the descriptor ΔG_1. Figure 17b indicates that the associative distal and associative alternating mechanisms are preferred for strong and weak binding of the intermediate *NNH, respectively. Close to the apex of the volcano plot, surface reactions in terms of *NNH → M−NNH_2 or $^*NHNH_2 \rightarrow {}^*NH_2NH_2$ govern the rate of the reaction rather than the formation of NH_3 or of the *NNH adsorbate, the steps of which are kinetically limiting at the volcano legs in agreement with the thermodynamic picture of the PDS.

In conclusion, the concept of $G_{max}(\eta)$ has deepened our understanding of the NRR over transition-metal oxides by outlining a change in the preferred mechanistic description and the limiting reaction steps at the volcano apex. These insights cannot be resolved by the notion of η_{TD} and go beyond thermodynamic considerations at the equilibrium potential, thus illustrating the advantages of the application of $G_{max}(\eta)$ for an understanding of trends and limiting steps in a class of materials.

4. CONCLUSIONS AND OUTLOOK

Computational electrochemistry[139−148] addressing electrified solid/liquid interfaces can be broadly classified into three categories: (a) first-principles or continuum model studies of the electric double layer at the interface,[149−152] (b) method development to move from a constant-charge description, as encountered with the computational hydrogen electrode approach, to a constant-potential formalism,[153−155] and (c) computational electrocatalysis by focusing on the energetics of the elementary reaction steps, thereby applying heuristic tools

https://doi.org/10.1021/acscatal.2c03997
ACS Catal. 2023, 13, 1740−1758

to quantify electrocatalytic activity.[84,156] The present perspective primarily addresses the last category while not explicitly focusing on the other two, yet highly important, research fields. We have aimed to provide an overview on the descriptor $G_{max}(\eta)$ for the heuristic materials screening of electrode compositions for electrochemical processes with applications to energy conversion and storage. For almost two decades, the theoretical community in electrocatalysis has made extensive use of the thermodynamic overpotential, η_{TD}, as an activity measure by discussing thermodynamically limiting reaction steps, denoted as the potential-determining step (PDS). To the best of our knowledge, the concept of $G_{max}(\eta)$ is the first attempt to go beyond a pure thermodynamic treatment of the elementary reaction steps when using heuristic analyses. We have introduced the mathematical formalism of $G_{max}(\eta)$ (cf. section 2.1) and illustrated the advantages of $G_{max}(\eta)$ compared to η_{TD} relating to the assessment of chemical reaction steps in the analysis of mechanistic pathways (cf. section 2.2). The notion of $G_{max}(\eta)$ can be further used within a microkinetic approach to approximate current densities (cf. section 2.3) or to resolve the rate-determining reaction step (RDS) of a reaction mechanism if the Tafel slope is predetermined (cf. section 2.4), thereby considering the approximations made within the free-energy span model (cf. section 2.5). We have discussed these aspects on four selected examples, namely breaking the scaling relation in the oxygen evolution reaction (OER) (cf. section 3.1), introducing a new method to determine the bifunctional index (BI) for the reversible oxygen electrocatalysis from theory (cf. section 3.2), comprehending a selectivity problem by the descriptor $G_{max}(\eta)$ (cf. section 3.3) and resolving the RDS for the nitrogen reduction reaction (NRR) over transition-metal oxides by $G_{max}(\eta)$ (cf. section 3.4).

As is evident from the above summary, so far, the application of the descriptor $G_{max}(\eta)$ has focused on comprehending the activity or selectivity of electrode compositions.[61,64,66,89,120,157] The stability aspect of electrocatalysts is often overlooked from the viewpoint of theory, which is mainly related to the fact that powerful concepts to understand degradation processes are yet missing, albeit urgently needed.[158−160] Hitherto, mainly bulk-related properties have been used to comprehend catalyst stability on the atomic scale.[161,162] This picture is, of course, rather simplistic because chemical information on the decomposition products would be required to gain a profound insight into catalyst degradation. A major step forward in this regard represents a recent study by Andreussi and co-workers, who modeled the oxygen evolution and reduction reactions over two-dimensional transition-metal dichalcogenides in conjunction with different decomposition pathways for highly active OER materials.[163] An overview of the suggested degradation steps is given in Figure 18.

As is evident from Figure 18, the formation of decomposition products such as X−O or X−O_2 (X = chalcogen) may comprise both electrochemical and chemical steps. This is where the descriptor $G_{max}(\eta)$ may come into play by determining the energetics of the degradation pathways dependent on the driving force, which ultimately can be compared to the free-energy span governing $G_{max}(\eta)$ for the elementary steps of product formation. The competition between decomposition and product formation can be seen as two different reaction channels, thus giving rise to a selectivity-type analysis as discussed in section 3.3. More precisely, this would allow extending current activity−selectivity investigations of electrocatalytic processes to more refined activity−selectivity−stability studies and allows the inclusion of stability investigations of electrode materials in the high-throughput screening of electrocatalysts at moderate computational costs. Comprehending the stability of electrocatalysts is of pivotal importance in theoretical studies and may advance screening activities in electrocatalysis,[51] particularly with respect to the OER, where catalyst stability is the major bottleneck in acidic electrolytes,[164] to the next level. We conclude that the concept of $G_{max}(\eta)$, based on the free-energy span model, may contribute to extend our understanding of catalyst stability for electrocatalytic processes at electrified solid/liquid interfaces in the next few years, and the gained insight may spur the design of equally active and stable electrode coatings for energy conversion and storage processes.

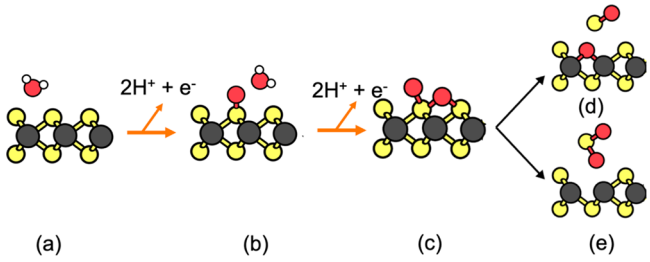

Figure 18. Schematic representation of the decomposition pathway for the formation of aqueous products (X−O and X−O_2) in the presence of an applied electrode potential. The initial steps denoted by orange arrows are of electrochemical nature, and the steps denoted by black arrows correspond to chemical processes. Transition metal and chalcogen (X = S, Se, or Te) atoms are visualized in gray and yellow, respectively. Figure adopted with permission from ref 163.

AUTHOR INFORMATION

Corresponding Author

Kai S. Exner − *University Duisburg-Essen, Faculty of Chemistry, Theoretical Inorganic Chemistry, 45141 Essen, Germany; Cluster of Excellence RESOLV, 44801 Bochum, Germany; Center for Nanointegration (CENIDE) Duisburg-Essen, 47057 Duisburg, Germany;* orcid.org/0000-0003-2934-6075; Email: kai.exner@uni-due.de

Author

Samad Razzaq − *University Duisburg-Essen, Faculty of Chemistry, Theoretical Inorganic Chemistry, 45141 Essen, Germany*

Complete contact information is available at: https://pubs.acs.org/10.1021/acscatal.2c03997

Notes

The authors declare no competing financial interest.

ACKNOWLEDGMENTS

K.S.E. acknowledges funding by the Ministry of Culture and Science of the Federal State of North Rhine-Westphalia (NRW Return Grant). K.S.E. is associated with the CRC/TRR247: "Heterogeneous Oxidation Catalysis in the Liquid Phase" (Project number 388390466-TRR 247), the RESOLV Cluster of Excellence, funded by the Deutsche Forschungsgemeinschaft under Germany's Excellence Strategy−EXC 2033−390677874−RESOLV, and the Center for Nanointegration (CENIDE). This article is based upon the work from COST

https://doi.org/10.1021/acscatal.2c03997
ACS Catal. 2023, 13, 1740−1758

Action 18234, supported by COST (European Cooperation in Science and Technology).

REFERENCES

(1) Siirola, J. J. Speculations on global energy demand and supply going forward. *Curr. Opin. Chem. Eng.* **2014**, *5*, 96−100.
(2) International Energy Agency: Key World Energy Statistics, 2021, https://www.iea.org/reports/key-world-energy-statistics-2021 (accessed Oct 26th, 2022).
(3) Sorrell, S. Reducing energy demand: A review of issues, challenges and approaches. *Renew. Sustain. Energy Rev.* **2015**, *47*, 74−82.
(4) Chen, J. G.; Crooks, M. R.; Seefeldt, L. C.; Bren, K. L. R.; Bullock, R. M.; Darensbourg, M. Y.; Holland, P. L.; Hoffman, B.; Janik, M. J.; Jones, A. K.; et al. Beyond fossil fuel-driven nitrogen transformations. *Science* **2018**, *360*, 873.
(5) Crabtree, G. W.; Dresselhaus, M. S.; Buchanan, M. V. The hydrogen economy. *Phys. Today* **2004**, *57*, 39−44.
(6) Esswein, A. J.; Nocera, D. G. Hydrogen production by molecular photocatalysis. *Chem. Rev.* **2007**, *107*, 4022−4047.
(7) Ibrahim, H.; Ilinca, A. P. J.; Perron, J. Energy storage systems-characteristics and comparisons. *Renew. Sustain. Energy Rev.* **2008**, *12*, 1221−1250.
(8) Choi, J. W.; Aurbach, D. Promise and reality of post-lithium-ion batteries with high energy densities. *Nat. Rev. Mater.* **2016**, *1*, 16013.
(9) Lee, J. S.; Kim, S. T.; Cao, R.; Choi, N. S.; Liu, M.; Lee, K. T.; Cho, J. Metal-air batteries with high energy density: Li-Air versus Zn-Air. *Adv. Energy Mater.* **2011**, *1*, 34−50.
(10) Carmo, M.; Fritz, D. L.; Mergel, J.; Stolten, D. A comprehensive review on PEM water electrolysis. *Int. J. Hydrog. Energy* **2013**, *38*, 4901−4934.
(11) Bandarenka, A. S.; Koper, M. T. M. Structural and electronic effects in heterogeneous electrocatalysis: Toward a rational design of electrocatalysts. *J. Catal.* **2013**, *308*, 11−24.
(12) Symes, M. D.; Cronin, L. Decoupling hydrogen and oxygen evolution during electrolytic water splitting using an electron-coupled-proton buffer. *Nat. Chem.* **2013**, *5*, 403−409.
(13) Sharaf, O. Z.; Orhan, M. F. An overview of fuel cell technology: Fundamentals and applications. *Renew. Sustain. Energy Rev.* **2014**, *32*, 810−853.
(14) Standaert, F.; Hemmes, K.; Woudstra, N. Analytical fuel cell modeling. *J. Power Sources* **1996**, *63*, 221−234.
(15) Wang, C. Y. Fundamental models for fuel cell engineering. *Chem. Rev.* **2004**, *104*, 4727−4766.
(16) Exner, K. S.; Sohrabnejad-Eskan, I.; Over, H. A universal approach to determine the free energy diagram of an electrocatalytic reaction. *ACS Catal.* **2018**, *8*, 1864−1879.
(17) Exner, K. S.; Over, H. Beyond the rate-determining step in the oxygen evolution reaction over a single-crystalline IrO_2(110) model electrode: Kinetic scaling relations. *ACS Catal.* **2019**, *9*, 6755−6765.
(18) Nørskov, J. K.; Rossmeisl, J.; Logadottir, A.; Lindqvist, L.; Kitchin, J.; Bligaard, T.; Jonsson, J. H. Origin of the overpotential for oxygen reduction at a fuel-cell cathode. *J. Phys. Chem. B* **2004**, *108*, 17886−17892.
(19) Nørskov, J. K.; Bligaard, T.; Logadottir, A.; Kitchin, J. R.; Chen, J. G.; Pandelov, S.; Stimming, U. Trends in the exchange current for hydrogen evolution. *J. Electrochem. Soc.* **2005**, *152*, J23−J26.
(20) Newns, D. M. Self-consistent model of hydrogen chemisorption. *Phys. Rev.* **1969**, *178*, 1123.
(21) Rossmeisl, J.; Logadottir, A.; Nørskov, J. K. Electrolysis of water on (oxidized) metal surfaces. *Chem. Phys.* **2005**, *319*, 178−184.
(22) Rossmeisl, J.; Qu, Z. W.; Zhu, H.; Kroes, G.-J.; Nørskov, J. K. Electrolysis of water on oxide surfaces. *J. Electroanal. Chem.* **2007**, *607*, 83−89.
(23) Groß, A. Grand-canonical approaches to understand structures and processes at electrochemical interfaces from an atomistic perspective. *Curr. Opin Electrochem* **2021**, *27*, 100684.
(24) Groß, A. Reversible vs standard hydrogen electrode scale in interfacial electrochemistry from a theoretician's atomistic point of view. *J. Phys. Chem. C* **2022**, *126*, 11439−11446.
(25) Exner, K. S.; Anton, J.; Jacob, T.; Over, H. Chlorine evolution reaction on RuO_2(110): Ab initio atomistic thermodynamics study - Pourbaix diagrams. *Electrochim. Acta* **2014**, *120*, 460−466.
(26) Sabatier, P. *La Catalyse en Chimie Organique*; Librarie Polytechnique: 1913.
(27) Ooka, H.; Huang, J.; Exner, K. S. The Sabatier principle in electrocatalysis: Basics, limitations, and extensions. *Front. Energy Res.* **2021**, *9*, 654460.
(28) van Santen, R. A.; Neurock, M.; Shetty, S. G. Reactivity theory of transition-metal surfaces: A Brønsted-Evans-Polanyi linear activation energy-free-energy analysis. *Chem. Rev.* **2010**, *110*, 2005−2048.
(29) Tsai, C.; Pedersen, F. A.; Nørskov, J. K. Tuning the MoS_2 edge-site activity for hydrogen evolution via support interactions. *Nano Lett.* **2014**, *14*, 1381−1387.
(30) Li, H.; Tsai, C.; Koh, A. L.; Cai, L.; Contryman, A. W.; Fragapane, A. H.; Zhao, J.; Han, H. S.; Manoharan, H. C.; Pedersen, F. A.; Nørskov, J. K.; Zheng, X. Activating and optimizing MoS_2 basal planes for hydrogen evolution through the formation of strained sulphur vacancies. *Nat. Mater.* **2016**, *15*, 48−53.
(31) Hong, X.; Chan, K.; Tsai, C.; Nørskov, J. K. How doped MoS_2 breaks transition-metal scaling relations for CO_2 electrochemical reduction. *ACS Catal.* **2016**, *6*, 4428−4437.
(32) Tsai, C.; Li, H.; Park, S.; Park, J.; Han, H. S.; Nørskov, J. K.; Zheng, X.; Pedersen, F. A. Electrochemical generation of sulfur vacancies in the basal plane of MoS_2 for hydrogen evolution. *Nat. Commun.* **2017**, *8*, 15113.
(33) Jaramillo, T. F.; Jørgensen, K. P.; Bonde, J.; Nielsen, J. H.; Horch, S.; Chorkendorff, I. Identification of active edge sites for electrochemical H_2 evolution from MoS_2 nanocatalysts. *Science* **2007**, *317*, 100−102.
(34) Chen, Z.; Cummins, D.; Reinecke, B. N.; Clark, E.; Sunkara, M. K.; Jaramillo, T. F. Core-shell MoO_3-MoS_2 nanowires for hydrogen evolution: A functional design for electrocatalytic materials. *Nano Lett.* **2011**, *11*, 4168−4175.
(35) Kibsgaard, J.; Chen, Z.; Reinecke, B. N.; Jaramillo, T. F. Engineering the surface structure of MoS_2 to preferentially expose active edge sites for electrocatalysis. *Nat. Mater.* **2012**, *11*, 963−969.
(36) Seitz, L. C.; Dickens, C. F.; Nishio, K.; Hikita, Y.; Montoya, J.; Doyle, A.; Kirk, C.; Vojvodic, A.; Hwang, H. Y.; Norskov, J. K.; Jaramillo, T. F. A highly active and stable IrO_x/$SrIrO_3$ catalyst for the oxygen evolution reaction. *Science* **2016**, *353*, 1011−1014.
(37) Schmickler, W.; Trasatti, S. Comment on "Trends in the exchange current for hydrogen evolution"[J. Electrochem. Soc., 152, J23 (2005)]. *J. Electrochem. Soc.* **2006**, *153*, L31−L32.
(38) Quaino, P.; Juarez, F.; Santos, E.; Schmickler, W. Volcano plots in hydrogen electrocatalysis - uses and abuses. *Beilstein J. Nanotechnol.* **2014**, *5*, 846−854.
(39) Kuo, D.-Y.; Paik, H.; Kloppenburg, J.; Faeth, B.; Shen, K. M.; Schlom, D. G.; Hautier, G.; Suntivich, J. Measurements of oxygen electroadsorption energies and oxygen evolution reaction on RuO_2(110): A discussion of the Sabatier principle and its role in electrocatalysis. *J. Am. Chem. Soc.* **2018**, *140*, 17597−17605.
(40) Chen, J.; Chen, Y.; Li, P.; Wen, Z.; Chen, S. Energetic span as a rate-determining term for electrocatalytic volcanos. *ACS Catal.* **2018**, *8*, 10590−10598.
(41) Koper, M. T. M. Analysis of electrocatalytic reaction schemes: Distinction between rate-determining and potential-determining steps. *J. Solid State Electrochem* **2013**, *17*, 339−344.
(42) Koper, M. T. M. Theory of multiple proton-electron transfer reactions and its implications for electrocatalysis. *Chem. Sci.* **2013**, *4*, 2710−2713.
(43) Exner, K. S. A universal descriptor for the screening of electrode materials for multiple-electron processes: Beyond the thermodynamic overpotential. *ACS Catal.* **2020**, *10*, 12607−12617.

https://doi.org/10.1021/acscatal.2c03997
ACS Catal. 2023, 13, 1740−1758

(44) Busch, M. Water oxidation: From mechanisms to limitations. *Curr. Opin Electrochem* **2018**, *9*, 278−284.
(45) Wodrich, M. D.; Sawatlon, B.; Busch, M.; Corminboeuf, C. On the generality of molecular volcano plots. *ChemCatChem.* **2018**, *10*, 1586−1591.
(46) Craig, M. J.; Coulter, G.; Dolan, E.; Soriano-López, J.; Mates-Torres, E.; Schmitt, W.; García-Melchor, M. Universal scaling relations for the rational design of molecular water oxidation catalysts with near-zero overpotential. *Nat. Commun.* **2019**, *10*, 4993.
(47) Craig, M. J.; García-Melchor, M. Reaction descriptors for the oxygen evolution reaction: Recent advances, challenges, and opportunities. *Curr. Opin Electrochem* **2022**, *35*, 101044.
(48) Exner, K. S. Comparison of the conventional volcano analysis with a unifying approach: Material screening based on a combination of experiment and theory. *J. Phys. Chem. C* **2020**, *124*, 822−828.
(49) Groenenboom, M. C.; Anderson, R. M.; Horton, D. J.; Basdogan, Y.; Roeper, D. F.; Policastro, S. A.; Keith, J. A. Doped amorphous Ti oxides to deoptimize oxygen reduction reaction catalysis. *J. Phys. Chem. C* **2017**, *121*, 16825−16830.
(50) Exner, K. S. Design criteria for oxygen evolution electrocatalysts from first principles: Introduction of a unifying material-screening approach. *ACS Appl. Energy Mater.* **2019**, *2*, 7991−8001.
(51) Exner, K. S. Recent progress in the development of screening methods to identify electrode materials for the oxygen evolution reaction. *Adv. Funct. Mater.* **2020**, *30*, 2005060.
(52) Chan, K.; Nørskov, J. K. Potential dependence of electrochemical barriers from ab initio calculations. *J. Phys. Chem. Lett.* **2016**, *7*, 1686−1690.
(53) Govindarajan, N.; Kastlunger, G.; Heenen, H. H.; et al. Improving the intrinsic activity of electrocatalysts for sustainable energy conversion: Where are we and where can we go? *Chem. Sci.* **2021**, *13*, 14.
(54) Karmodak, N.; Vijay, S.; Kastlunger, G.; Chan, K. Computational screening of single and di-atom catalysts for electrochemical CO_2 reduction. *ACS Catal.* **2022**, *12*, 4818−4824.
(55) Tayyebi, E.; Abghoui, Y.; Skúlason, E. Elucidating the mechanism of electrochemical N_2 reduction at the Ru(0001) electrode. *ACS Catal.* **2019**, *9*, 11137−11145.
(56) Kozuch, S.; Shaik, S. How to conceptualize catalytic cycles? The Energetic span model. *Acc. Chem. Res.* **2011**, *44*, 101−110.
(57) Kozuch, S. A refinement of everyday thinking: The energetic span model for kinetic assessment of catalytic cycles. *WIREs Comput. Mol. Sci.* **2012**, *2*, 795−815.
(58) Exner, K. S. Why approximating electrocatalytic activity by a single free-energy change is insufficient. *Electrochim. Acta* **2021**, *375*, 137975.
(59) Govindarajan, N.; Garcia-Lastra, J. M.; Meijer, E. J.; Calle-Vallejo, F. Does the breaking of adsorption-energy scaling relations guarantee enhanced electrocatalysis? *Curr. Opin Electrochem* **2018**, *8*, 110−117.
(60) Exner, K. S. The electrochemical-step asymmetry index. *MethodsX* **2021**, *8*, 101590.
(61) Exner, K. S. Why the optimum thermodynamic free-energy landscape of the oxygen evolution reaction reveals an asymmetric shape. *Mater. Today Energy* **2021**, *21*, 100831.
(62) Exner, K. S.; Over, H. Kinetics of electrocatalytic reactions from first-principles: A critical comparison with the ab initio thermodynamics approach. *Acc. Chem. Res.* **2017**, *50*, 1240−1247.
(63) Exner, K. S. On the optimization of nitrogen-reduction electrocatalysts: Breaking scaling relation or catalytic resonance theory? *ChemCatChem.* **2022**, *14*, No. e202200366.
(64) Razzaq, S.; Exner, K. S. Method to determine the bifunctional index for the oxygen electrocatalysis from theory. *ChemElectroChem.* **2022**, *9*, No. e202101603.
(65) Binninger, T.; Doublet, M.-L. The Ir-OOOO-Ir transition state and the mechanism of the oxygen evolution reaction on IrO_2(110). *Energy Environ. Sci.* **2022**, *15*, 2519.
(66) Exner, K. S. Why the breaking of the OOH versus OH scaling relation might cause decreased electrocatalytic activity. *Chem. Catalysis* **2021**, *1*, 258−271.
(67) Pique, O.; Illas, F.; Calle-Vallejo, F. Designing water splitting catalysts using rules of thumb: Advantages, dangers and alternatives. *Phys. Chem. Chem. Phys.* **2020**, *22*, 6797−6803.
(68) Bockris, J. O'M.; Reddy, A. K. N. *Modern Electrochemistry*, Vol. *2*; Plenum Publishing: 1973; pp 991−1014.
(69) Man, I. C.; Su, H.-Y.; Calle-Vallejo, F.; Hansen, H. A.; Martinez, J. I.; Inoglu, N. G.; Kitchin, J.; Jaramillo, T. F.; Nørskov, J. K.; Rossmeisl, J. Universality in oxygen evolution electrocatalysis on oxide surfaces. *ChemCatChem.* **2011**, *3*, 1159−1165.
(70) Fletcher, S. Tafel slopes from first principles. *J. Solid State Electrochem* **2009**, *13*, 537−549.
(71) Fang, Y.-H.; Liu, Z.-P. Tafel kinetics of electrocatalytic reactions: From experiment to first-principles. *ACS Catal.* **2014**, *4*, 4364−4376.
(72) Sumaria, V.; Krishnamurthy, D.; Viswanathan, V. Quantifying confidence in DFT predicted surface pourbaix diagrams and associated reaction pathways for chlorine evolution. *ACS Catal.* **2018**, *8*, 9034−9042.
(73) Markovic, N. M.; Grgur, B. N.; Ross, P. N. Temperature-dependent hydrogen electrochemistry on platinum low-index single-crystal surfaces in acid solutions. *J. Phys. Chem. B* **1997**, *101*, 5405−5413.
(74) Sohrabnejad-Eskan, I.; Goryachev, A.; Exner, K. S.; Kibler, L. A.; Hensen, E. J. M.; Hofmann, J. M.; Over, H. Temperature-dependent kinetic studies of the chlorine evolution reaction over RuO_2(110) model electrodes. *ACS Catal.* **2017**, *7*, 2403−2411.
(75) Koper, M. T. M. Thermodynamic theory of multi-electron transfer reactions: Implications for electrocatalysis. *J. Electroanal. Chem.* **2011**, *660*, 254−260.
(76) Viswanathan, V.; Hansen, H. A. Unifying solution and surface electrochemistry: Limitations and opportunities in surface electrocatalysis. *Top. Catal.* **2014**, *57*, 215−221.
(77) Mom, R. V.; Cheng, J.; Koper, M. T. M.; Sprik, M. Modeling the oxygen evolution reaction on metal oxides: The Influence of unrestricted DFT calculations. *J. Phys. Chem. C* **2014**, *118*, 4095−4102.
(78) Calle-Vallejo, F.; Krabbe, A.; García-Lastra, J. M. How covalence breaks adsorption-energy scaling relations and solvation restores them. *Chem. Sci.* **2017**, *8*, 124−130.
(79) Christensen, R.; Hansen, H. A.; Dickens, C. F.; Nørskov, J. K.; Vegge, T. Functional independent scaling relation for ORR/OER catalysts. *J. Phys. Chem. C* **2016**, *120*, 24910−24916.
(80) Halck, N. B.; Petrykin, V.; Krtil, P.; Rossmeisl, J. Beyond the volcano limitations in electrocatalysis-oxygen evolution reaction. *Phys. Chem. Chem. Phys.* **2014**, *16*, 13682−13688.
(81) Perez-Ramirez, J.; Lopez, N. Strategies to break linear scaling relationships. *Nat. Catal.* **2019**, *2*, 971−976.
(82) Govindarajan, N.; Koper, M. T. M.; Meijer, E. J.; Calle-Vallejo, F. Outlining the scaling-based and scaling-free optimization of electrocatalysts. *ACS Catal.* **2019**, *9*, 4218−4225.
(83) Ooka, H.; Nakamura, R. Shift of the optimum binding energy at higher rates of catalysis. *J. Phys. Chem. Lett.* **2019**, *10*, 6706−6713.
(84) Exner, K. S. Does a thermoneutral electrocatalyst correspond to the apex of a volcano plot for a simple two-electron process? *Angew. Chem., Int. Ed.* **2020**, *59*, 10236−10240.
(85) Exner, K. S. Paradigm change in hydrogen electrocatalysis: The volcano's apex is located at weak bonding of the reaction intermediate. *Int. J. Hydrog.* **2020**, *45*, 27221−27229.
(86) Lindgren, P.; Kastlunger, G.; Peterson, A. A. A challenge to the G ∼ 0 interpretation of hydrogen evolution. *ACS Catal.* **2020**, *10*, 121−128.
(87) Dickens, C. F.; Kirk, C.; Nørskov, J. K. Insights into the electrochemical oxygen evolution reaction with ab initio calculations and microkinetic modeling: Beyond the limiting potential volcano. *J. Phys. Chem. C* **2019**, *123*, 18960−18977.

https://doi.org/10.1021/acscatal.2c03997
ACS Catal. 2023, 13, 1740−1758

(88) Zhang, Y.; Zhang, J.; Huang, J. Potential-dependent volcano plot for oxygen reduction: Mathematical origin and implications for catalyst design. *J. Phys. Chem. Lett.* **2019**, *10*, 7037−7043.
(89) Razzaq, S.; Exner, K. S. Statistical analysis of breaking scaling relation in the oxygen evolution reaction. *Electrochim. Acta* **2022**, *412*, 140125.
(90) Divanis, S.; Kutlusoy, T.; Boye, I. M. I.; Man, I. C.; Rossmeisl, J. Oxygen evolution reaction: a perspective on a decade of atomic scale simulations. *Chem. Sci.* **2020**, *11*, 2943−2950.
(91) Nishimoto, T.; Shinagawa, T.; Naito, T.; Takanabe, K. Microkinetic assessment of electrocatalytic oxygen evolution reaction over iridium oxide in unbuffered conditions. *J. Catal.* **2020**, *391*, 435−445.
(92) Rao, R. R.; Kolb, M. J.; Halck, N. B.; Pedersen, A. F.; Mehta, A.; You, H.; Stoerzinger, K. A.; Feng, Z.; Hansen, H. A.; Zhou, H.; et al. Towards identifying the active sites on RuO_2(110) in catalyzing oxygen evolution. *Energy Environ. Sci.* **2017**, *10*, 2626−2637.
(93) Rao, R. R.; Kolb, M. J.; Giordano, L.; Pedersen, A. F.; Katayama, Y.; Hwang, J.; Mehta, A.; You, H.; Lunger, J. R.; Zhou, H.; et al. Operando identification of site-dependent water oxidation activity on ruthenium dioxide single-crystal surfaces. *Nat. Catal.* **2020**, *3*, 516−525.
(94) Exner, K. S. Universality in oxygen evolution electrocatalysis: High-throughput screening and a priori determination of the rate-determining reaction step. *ChemCatChem.* **2020**, *12*, 2000−2003.
(95) Armstrong, A. R.; Bruce, P. G. Synthesis of layered $LiMnO_2$ as an electrode for rechargeable lithium batteries. *Nature* **1996**, *381*, 499−500.
(96) Janek, J.; Zeier, W. G. A solid future for battery development. *Nat. Energy* **2016**, *1*, 16141.
(97) Li, L.; Chang, Z.; Zhang, X. B. Recent progress on the development of metal-air Batteries. *Adv. Sustain. Syst.* **2017**, *1*, 1700036.
(98) Bruce, P. G.; Freunberger, S. A.; Hardwick, L. J.; Tarascon, J.-M. Li-O2 and Li-S batteries with high energy storage. *Nat. Mater.* **2012**, *11*, 19−29.
(99) Girishkumar, G.; McCloskey, B.; Luntz, A. C.; Swanson, S.; Wilcke, W. Lithium-Air Battery: Promise and Challenges. *J. Phys. Chem. Lett.* **2010**, *1*, 2193.
(100) Scrosati, B.; Hassoun, J.; Sun, Y.-K. Lithium-ion batteries. A look into the future. *Energy Environ. Sci.* **2011**, *4*, 3287.
(101) Jung, H.-Y.; Park, S.; Popov, B. N. Electrochemical studies of an unsupported PtIr electrocatalyst as a bifunctional oxygen electrode in a unitized regenerative fuel cell. *J. Power Sources* **2009**, *191*, 357−361.
(102) Huang, Z.-F.; Wang, J.; Peng, Y.; Jung, C.-Y.; Fisher, A.; Wang, X. Design of efficient bifunctional oxygen reduction/evolution electrocatalyst: Recent advances and perspectives. *Adv. Energy Mater.* **2017**, *7*, 1700544.
(103) Masa, J.; Xia, W.; Sinev, I.; Zhao, A.; Sun, Z.; Grützke, S.; Weide, P.; Muhler, M.; Schuhmann, W. Mn_xO_y/NC and Co_xO_y/NC nanoparticles embedded in a nitrogen-doped carbon matrix for high-performance bifunctional oxygen electrodes. *Angew. Chem., Int. Ed.* **2014**, *53*, 8508−8512.
(104) Gorlin, Y.; Jaramillo, T. F. A Bifunctional nonprecious metal catalyst for oxygen reduction and water oxidation. *J. Am. Chem. Soc.* **2010**, *132*, 13612−13614.
(105) Scholz, F. *Electroanalytical Methods*; Springer: 2014.
(106) Kolb, M. J.; Calle-Vallejo, F. The bifunctional volcano plot: Thermodynamic limits for single-atom catalysts for oxygen reduction and evolution. *J. Mater. Chem. A* **2022**, *10*, 5937.
(107) Tao, H. B.; Zhang, J.; Chen, J.; Zhang, L.; Xu, Y.; Chen, J. G.; Liu, B. Revealing energetics of surface oxygen redox from kinetic fingerprint in oxygen electrocatalysis. *J. Am. Chem. Soc.* **2019**, *141*, 13803−13811.
(108) Dionigi, F.; Zeng, Z.; Sinev, I.; Merzdorf, T.; Deshpande, S.; Lopez, M. B.; Kunze, S.; Zegkinoglou, I.; Sarodnik, H.; Fan, D.; et al. In-situ structure and catalytic mechanism of NiFe and CoFe layered double hydroxides during oxygen evolution. *Nat. Commun.* **2020**, *11*, 2522.
(109) Dionigi, F.; Zhu, J.; Zeng, Z.; Merzdorf, T.; Sarodnik, H.; Gliech, M.; Pan, L.; Li, W.-X.; Greeley, J.; Strasser, P. Intrinsic electrocatalytic activity for oxygen evolution of crystalline 3d-transition metal layered double hydroxides. *Angew. Chem., Int. Ed.* **2021**, *60*, 14446−14457.
(110) Retuerto, M.; Calle-Vallejo, F.; Pascual, L.; Lumbeeck, G.; Fernandez-Diaz, M. T.; Croft, M.; Gopalakrishnan, J.; Peña, M. A.; Hadermann, J.; Greenblatt, M.; Rojas, S. $La_{1.5}Sr_{0.5}NiMn_{0.5}Ru_{0.5}O_6$ double perovskite with enhanced ORR/OER bifunctional catalytic activity. *ACS Appl. Mater. Interfaces* **2019**, *11*, 21454−21464.
(111) Jiang, Y.; Ni, P.; Chen, C.; Lu, Y.; Yang, P.; Kong, B.; Fisher, A.; Wang, X. Selective electrochemical H_2O_2 production through two-electron oxygen electrochemistry. *Adv. Energy Mater.* **2018**, *8*, 1801909.
(112) Viswanathan, V.; Hansen, H. A.; Nørskov, J. K. Selective electrochemical generation of hydrogen peroxide from water oxidation. *J. Phys. Chem. Lett.* **2015**, *6*, 4224−4228.
(113) Kelly, S. R.; Shi, X.; Back, S.; Vallez, L.; Park, S. Y.; Siahrostami, S.; Zheng, X.; Nørskov, J. K. ZnO as an active and selective catalyst for electrochemical water oxidation to hydrogen peroxide. *ACS Catal.* **2019**, *9*, 4593−4599.
(114) Lee, T. H.; Park, S.; Choi, T. H.; Zhang, L.; Kim, J.; Guo, J.; Park, H. B.; Kim, W.; Kim, H. W. Detailed characterization of an annealed reduced graphene oxide catalyst for selective peroxide formation activity. *ACS Appl. Mater. Interfaces* **2020**, *12*, 46439−46445.
(115) Muzyka, K.; Sun, J.; Fereja, T. H.; Lan, Y.; Zhang, W.; Xu, G. Boron-doped diamond: Current progress and challenges in view of electroanalytical applications. *Anal. Methods* **2019**, *11*, 397−414.
(116) Suo, N.; Huang, H.; Wu, A.; Cao, G.; Hou, X.; Zhang, G. Porous boron doped diamonds as metal-free catalysts for the oxygen reduction reaction in alkaline solution. *Appl. Surf. Sci.* **2018**, *439*, 329−335.
(117) Mavrikis, S.; Göltz, M.; Rosiwal, S.; Wang, L.; Ponce de León, C. Boron-doped diamond electrocatalyst for enhanced anodic H_2O_2 production. *ACS Appl. Energy Mater.* **2020**, *3*, 3169−3173.
(118) Wyckoff, R. W. G. Crystal structures. *Acta Crystallogr.* **1965**, *18*, 129−139.
(119) Garcia-Miranda Ferrari, A.; Brownson, D. A. C.; Banks, C. E. Investigating the Integrity of graphene towards the electrochemical oxygen evolution reaction. *ChemElectroChem.* **2019**, *6*, 5446−5453.
(120) Ivanova, A.; Chesnokov, A.; Bocharov, D.; Exner, K. S. A universal approach to quantify overpotential-dependent selectivity trends for the competing oxygen evolution and peroxide formation reactions: A case study on graphene model electrodes. *J. Phys. Chem. C* **2021**, *125*, 10413−10421.
(121) Almeida, M. O.; Kolb, M. J.; Lanza, M. R. V.; Illas, F.; Calle-Vallejo, F. Gas-phase errors affect DFT-based electrocatalysis models of oxygen reduction to hydrogen peroxide. *ChemElectroChem.* **2022**, *9*, No. e202200210.
(122) Exner, K. S. Design criteria for the competing chlorine and oxygen evolution reactions: Avoid the OCl adsorbate to enhance chlorine selectivity. *Phys. Chem. Chem. Phys.* **2020**, *22*, 22451−22458.
(123) Brønsted, J. Acid and basic catalysis. *Chem. Rev.* **1928**, *5*, 231−338.
(124) Cheng, J.; Hu, P.; et al. Brønsted-Evans-Polanyi relation of multistep reactions and volcano curve in heterogeneous catalysis. *J. Phys. Chem. C* **2008**, *112*, 1308−1311.
(125) Exner, K. S. Controlling stability and selectivity in the competing chlorine and oxygen evolution reaction over transition metal oxide electrodes. *ChemElectroChem.* **2019**, *6*, 3401−3409.
(126) Perry, S. C.; Pangotra, D.; Vieira, L.; Csepei, L.-I.; Sieber, V.; Wang, L.; Ponce de León, C.; Walsh, F. C. Electrochemical synthesis of hydrogen peroxide from water and oxygen. *Nat. Rev. Chem.* **2019**, *3*, 442−458.
(127) Huang, B.; Wu, Y.; Chen, B.; Qian, Y.; Zhou, N.; Li, N. Transition-metal-atom-pairs deposited on g-CN monolayer for

https://doi.org/10.1021/acscatal.2c03997
ACS Catal. 2023, 13, 1740−1758

nitrogen reduction reaction: Density functional theory calculations. *Chin. J. Catal.* **2021**, *42*, 1160−1167.
(128) Smil, V. Global population and the nitrogen cycle. *Sci. Am.* **1997**, *277*, 76.
(129) Nielsen, A. *Ammonia: Catalysis and manufacture, in ammonia synthesis over non-iron catalysts and related phenomena*; Springer: 1995; Vol. *103*, pp 103−148.
(130) Ren, Y.; Yu, C.; Tan, X.; Huang, H.; Wei, Q.; Qiu, J. Strategies to suppress hydrogen evolution for highly selective electrocatalytic nitrogen reduction: Challenges and perspectives. *Energy Environ. Sci.* **2021**, *14*, 1176−1193.
(131) Guo, C.; Ran, J.; Vasileff, A.; Qiao, S. Z. Rational design of electrocatalysts and photo(electro)catalysts for nitrogen reduction to ammonia (NH_3) under ambient conditions. *Energy Environ. Sci.* **2018**, *11*, 45−56.
(132) Singh, A. R.; Rohr, B. A.; Schwalbe, J. A.; Cargnello, M.; Chan, K.; Jaramillo, T. F.; Chorkendorff, I.; Nørskov, J. K. Electrochemical ammonia synthesis-the selectivity challenge. *ACS Catal.* **2017**, *7*, 706−709.
(133) Dražević, E.; Skúlason, E. Are there any overlooked catalysts for electrochemical NH_3 synthesis-new insights from analysis of thermochemical data. *iScience* **2020**, *23*, 101803.
(134) Höskuldsson, Á. B.; Abghoui, Y.; Gunnarsdóttir, A. B.; Skúlason, E. Computational screening of rutile oxides for electrochemical ammonia formation. *ACS Sustain. Chem. Eng.* **2017**, *5*, 10327−10333.
(135) Skúlason, E.; Bligaard, T.; Gudmundsdóttir, S.; Studt, F.; Rossmeisl, J.; Abild-Pedersen, F.; Vegge, T.; Jónsson, H.; Nørskov, J. K. A theoretical evaluation of possible transition metal electrocatalysts for N_2 reduction. *Phys. Chem. Chem. Phys.* **2012**, *14*, 1235−1245.
(136) Exner, K. S. Beyond the thermodynamic volcano picture in the nitrogen reduction reaction over transition-metal oxides: Implications for materials screening. *Chin. J. Catal.* **2022**, *43*, 2871−2880.
(137) Urrego-Ortiz, R.; Builes, S.; Calle-Vallejo, F. Impact of intrinsic density functional theory errors on the predictive power of nitrogen cycle electrocatalysis models. *ACS Catal.* **2022**, *12*, 4784−4791.
(138) Bao, D.; Zhang, Q.; Meng, F.-L.; Zhong, H.-X.; Shi, M.-M.; Zhang, Y.; Yan, J.-M.; Jiang, Q.; Zhang, X.-B. Electrochemical reduction of N_2 under ambient conditions for artificial N_2 fixation and renewable energy storage using N_2/NH_3 cycle. *Adv. Mater.* **2017**, *29*, 1604799.
(139) Liao, P.; Keith, J. A.; Carter, E. A. Water oxidation on pure and doped hematite (0001) surfaces: Prediction of Co and Ni as effective dopants for electrocatalysis. *J. Am. Chem. Soc.* **2012**, *134*, 13296−13309.
(140) Steinmann, S. N.; Carine Miche, C. How to gain atomistic insights on reactions at the water/solid interface? *ACS Catal.* **2022**, *12*, 6294−6301.
(141) Abidi, N.; Lim, K. R. G.; Seh, Z. W.; Steinmann, S. N. Atomistic modeling of electrocatalysis: Are we there yet? *Comput. Mol. Sci.* **2021**, *11*, No. e1499.
(142) Abidi, N.; Steinmann, S. N. How are transition states modeled in heterogeneous electrocatalysis? *Curr. Opin Electrochem.* **2022**, *33*, 100940.
(143) Liu, J.-X.; Richards, D.; Singh, N.; Goldsmith, B. R. Activity and selectivity trends in electrocatalytic nitrate reduction on transition metals. *ACS Catal.* **2019**, *9*, 7052−7064.
(144) Ringe, S.; Hörmann, N. G.; Oberhofer, H.; Reute, K. Implicit solvation methods for catalysis at electrified interfaces. *Chem. Rev.* **2022**, *122*, 10777−10820.
(145) Román, A. M.; Dudoff, J.; Baz, A.; Holewinski, A. Identifying "Optimal" Electrocatalysts: Impact of operating potential and charge transfer model. *ACS Catal.* **2017**, *7*, 8641−8652.
(146) Back, S.; Tran, K.; Ulissi, Z. W. Toward a design of active oxygen evolution catalysts: Insights from automated density functional theory calculations and machine learning. *ACS Catal.* **2019**, *9*, 7651−7659.
(147) Hajiyani, H.; Pentcheva, R. Surface termination and composition control of activity of the $Co_xNi_{1-x}Fe_2O_4(001)$ surface for water oxidation: Insights from DFT+U calculations. *ACS Catal.* **2018**, *8*, 11773−11782.
(148) Hasan, M. H.; McCrum, I. T. Understanding the role of near-surface solvent in electrochemical adsorption and electrocatalysis with theory and experiment. *Curr. Opin Electrochem* **2022**, *33*, 100937.
(149) Le, J.-B.; Yang, X.-H.; Zhuang, Y.-B.; Jia, M.; Cheng, J. Recent progress toward Ab Initio modeling of electrocatalysis. *J. Phys. Chem. Lett.* **2021**, *12*, 8924−8931.
(150) Li, L.; Liu, Y.-P.; Le, J.-B.; Cheng, J. Unraveling molecular structures and ion effects of electric double layers at metal water interfaces. *Cell Rep. Phys. Sci.* **2022**, *3*, 100759.
(151) Le, J.-B.; Cheng, J. Modeling electrified metal/water interfaces from ab initio molecular dynamics: structure and Helmholtz capacitance. *Curr. Opin Electrochem* **2021**, *27*, 100693.
(152) Zhang, C.; Sayer, T.; Hutter, J.; Sprik, M. Modelling electrochemical systems with finite field molecular dynamics. *J. Phys. Energy* **2020**, *2*, 032005.
(153) Hörmann, N. G.; Marzari, N.; Reuter, K. Electrosorption at metal surfaces from first principles. *Npj Comput. Mater.* **2020**, *6*, 1−10.
(154) Kastlunger, G.; Lindgren, P.; Peterson, A. A. Controlled-potential simulation of elementary electrochemical reactions: Proton discharge on metal surfaces. *Phys. Chem. C* **2018**, *122*, 12771−12781.
(155) Van den Bossche, M.; Skulason, E.; Rose-Petruck, C.; Jonsson, H. Assessment of constant-potential implicit solvation calculations of electrochemical energy barriers for H_2 Evolution on Pt. *J. Phys. Chem. C* **2019**, *123*, 4116−4124.
(156) Nørskov, J. K.; Bligaard, T.; Rossmeisl, J.; Christensen, C. H. Towards the computational design of solid catalysts. *Nat. Chem.* **2009**, *1*, 37−46.
(157) Exner, K. S. On the lattice oxygen evolution mechanism: Avoiding pitfalls. *ChemCatChem.* **2021**, *13*, 4066−4074.
(158) Raman, A. S.; Vojvodic, A. Providing atomistic insights into the dissolution of rutile oxides in electrocatalytic water splitting. *J. Phys. Chem. C* **2022**, *126*, 922−932.
(159) Zagalskaya, A.; Alexandrov, V. Role of defects in the interplay between adsorbate evolving and lattice oxygen mechanisms of the oxygen evolution reaction in RuO_2 and IrO_2. *ACS Catal.* **2020**, *10*, 3650−3657.
(160) Zagalskaya, A.; Evazadde, I.; Alexandrov, V. Ab initio thermodynamics and kinetics of the lattice oxygen evolution reaction in iridium oxides. *ACS Energy Lett.* **2021**, *6*, 1124−1133.
(161) Castelli, I. E.; Thygesen, K. S.; Jacobsen, K. W. Calculated pourbaix diagrams of cubic perovskites for water splitting: Stability against corrosion. *Top. Catal.* **2014**, *57*, 265−272.
(162) Huang, L. F.; Scully, J. R.; Rondinelli, J. M. Modeling corrosion with first-principles electrochemical phase diagrams. *Annu. Rev. Mater. Res.* **2019**, *49*, 53−77.
(163) Karmodak, N.; Bursi, L.; Andreussi, O. Oxygen evolution and reduction on two-dimensional transition metal dichalcogenides. *J. Phys. Chem. Lett.* **2022**, *13*, 58−65.
(164) Weber, T.; Pfrommer, J.; Abb, M. J. S.; Herd, B.; Khalid, O.; Rohnke, M.; Lakner, P. H.; Evertsson, J.; Volkov, S.; Bertram, F.; Znaiguia, R.; Francesco, C.; Vonk, V.; Lundgren, E.; Stierle, A.; Over, H. Potential-induced pitting corrosion of an $IrO_2(110)$-$RuO_2(110)$/Ru(0001) Model electrode under oxygen evolution reaction conditions. *ACS Catal.* **2019**, *9*, 6530−6539.

https://doi.org/10.1021/acscatal.2c03997
ACS Catal. 2023, 13, 1740−1758